Andrejs Sabanskis

Gāzes plūsmas ietekmes uz zonas formu un piemaisījumu pārnesi modelēšana peldošās zonas procesā

Modeling of the influence of gas flow on the zone shape and dopant transport in floating zone process

Zinātnisko publikāciju kopa / Scientific papers

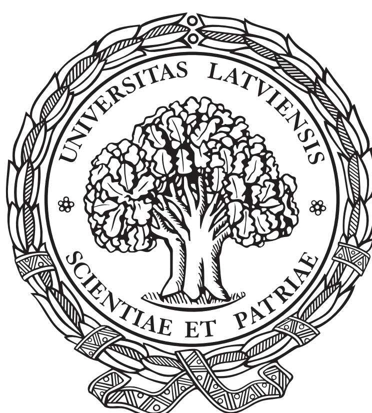

Latvijas Universitāte / University of Latvia

Rīga, 2015

Anotācija

Darbā tiek veikta silīcija monokristālu audzēšanas ar peldošās zonas metodi matemātiskā modelēšana. Izveidotais matemātiskais modelis ļauj aprēķināt gāzes plūsmu un tās radīto papildus dzesēšanu uz silīcija virsmām. Tāpat ir izveidots vienots modelis piemaisījumu pārnesei gāzē un kausējumā, kas apraksta piemaisījumu ievadīšanu no atmosfēras.

Jaunizveidotie modeļi tika sajūgti ar esošo modeļu sistēmu. Modeļu kopums realizēts datorprogrammu veidā, galvenokārt uz atvērtā koda bibliotēkas `OpenFOAM` bāzes. Tika veikti peldošās zonas procesa skaitliskie aprēķini, kuros pētīta gāzes un kausējuma plūsma un to ietekme uz silīcija fāzu robežvirsmām, kā arī piemaisījumu pārnese gāzē un kausējumā.

Abstract

In the present work mathematical modeling of floating zone silicon single crystal growth is carried out. The developed mathematical model allows to calculate the gas flow and additional cooling at silicon surfaces caused by it. Additionally, a unified model of the dopant transport in the gas and melt is developed, which describes doping from the atmosphere.

The developed models have been coupled with the existing system of models. The set of models is implemented in computer programs, mainly based on the open source library `OpenFOAM`. Numerical calculations of the floating zone process have been carried out in which gas and melt flow and their influence on the silicon phase boundaries as well as dopant transport in the gas and melt was investigated.

Promocijas darbā iekļauto publikāciju saraksts

List of scientific papers included in the Thesis

[dis1] A. Sabanskis, J. Virbulis. “Simulation of the influence of gas flow on melt convection and phase boundaries in FZ silicon single crystal growth”. *Journal of Crystal Growth* 417 (2015). Effect of natural and forced convection in materials crystallization, pp. 51–57.

[dis2] A. Sabanskis, K. Surovovs, A. Krauze, J. Virbulis. “Modelling of dopant transport during floating zone growth of silicon”. *Proceedings of the International Scientific Colloquium “Modelling for Electromagnetic Processing”* (2014), pp. 99–104.

[dis3] A. Sabanskis, K. Surovovs, J. Virbulis. “Three-dimensional modelling of dopant transport in gas and melt during FZ silicon crystal growth”. *Magnetohydrodynamics* 51.1 (2015), pp. 157–170.

[dis4] K. Surovovs, A. Muiznieks, A. Sabanskis, J. Virbulis. “Hydrodynamical aspects of the floating zone silicon crystal growth process”. *Journal of Crystal Growth* 401 (2014). Proceedings of 17th International Conference on Crystal Growth and Epitaxy (ICCGE-17), pp. 120–123.

[dis5] A. Sabanskis, K. Surovovs, A. Krauze, M. Plate, J. Virbulis. “Modelling of the influence of electromagnetic force on melt convection and dopant distribution during floating zone growth of silicon”. *Magnetohydrodynamics* (2015). Accepted.

Journal of Crystal Growth 417 (2015) 51–57

Contents lists available at ScienceDirect

Journal of Crystal Growth

journal homepage: www.elsevier.com/locate/jcrysgro

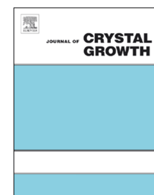

Simulation of the influence of gas flow on melt convection and phase boundaries in FZ silicon single crystal growth

A. Sabanskis*, J. Virbulis

Faculty of Physics and Mathematics, University of Latvia, Zellu Str. 8, LV-1002 Riga, Latvia

ARTICLE INFO

Available online 30 July 2014

Keywords:
A1. Computer simulation
A1. Convection
A1. Heat transfer
A1. Phase boundaries
A2. Floating zone technique
A2. Growth from melt

ABSTRACT

Axisymmetric calculations of inert gas flow in a floating zone puller are carried out using an open source software package OpenFOAM. Transient axisymmetric melt flow in liquid silicon and quasi-stationary shape of silicon phase boundaries are calculated using a specialized program FZone. Additional heat losses at silicon surfaces caused by the gas flow are taken into account for argon and helium, while maintaining the height of molten zone by adjusting inductor current. Cooling causes an increase of electromagnetic force, heat sources and more intense melt flow, while crystallization interface deflection decreases. The shear stress of gas flow is found to be an order of magnitude weaker than electromagnetic and Marangoni forces.

© 2014 Elsevier B.V. All rights reserved.

1. Introduction

During the growth of silicon (Si) single crystals with the floating zone (FZ) technique, an inert gas atmosphere consisting primarily of argon is commonly used [1,2]. To avoid electrical breakdown at the current suppliers of the inductor, according to Paschen's law, high enough gas pressure must be applied. The characteristic values of gas pressure are 1–3 bar, and the upper limit of pressure depends on a puller [3].

Mathematical models of the FZ process have been developed for about two decades, see, e.g., Refs. [4–7]. The considered physical phenomena include high-frequency (HF) electromagnetic (EM) field, thermal radiation, conductive heat transfer in crystals as well as non-stationary melt hydrodynamics (HD). The models typically calculate the axisymmetric shape of phase boundaries using quasi-stationary approach. Since the shape of solid–liquid and liquid–gas interfaces is unknown, specialized models exist for the calculation of free melt surface shape, the positions of crystallization and melting interfaces and open melting front.

However, only a few studies consider the influence of gas cooling. Larsen [5] uses an analytical estimation for the heat transfer coefficient, h. At the crystal surface, additional heat losses by gas flow are modeled by the q_{gas} term in the following equation:

$$q_{\mathrm{loss}} = q_{\mathrm{rad}} + q_{\mathrm{gas}}, \quad q_{\mathrm{gas}} = h(T_{\mathrm{c}} - T_{\mathrm{g}}) \tag{1}$$

Here q_{loss} is the heat flux density of heat losses, q_{rad} is the net radiation heat flux density, T_{c} is the local crystal surface temperature and T_{g} is the average gas temperature in a puller. For higher argon pressure the crystal cooling was stronger (i.e., larger value of h), and a decrease of crystallization interface deflection was observed both in simulations and experiment.

The same expression for additional heat losses at the crystal surface was used by Menzel [3]. For determining the coefficient h, fitting of simulation results and experimental temperature measurements for several points along the surface of a heated silicon rod was done.

Axisymmetric simulations of argon and helium flow during FZ growth of germanium have been carried out by Wünscher [8]. It was found that helium cooling is comparable to q_{rad} and is 8 times stronger than argon cooling. Nevertheless, the influence of gas cooling on phase boundaries was not considered.

Therefore, there are no investigations of FZ process in which both predict cooling power density of gas flow at all surfaces and take it into account for the calculation of melt flow and phase boundaries. The present work describes the model for gas flow calculations in FZ process, which allows us to calculate cooling heat flux densities at crystal, feed rod, open melting front and free melt surfaces. Gas cooling is then taken into account for the calculations of melt HD and phase boundaries.

It should be mentioned that the influence of gas flow in the Czochralski Si growth process is well studied, see, e.g., Ref. [9]. The gas flow conditions are completely different, as typical gas pressure is several tens of millibar, and the velocity of forced directed gas flow through a complex geometry is by an order of magnitude higher than in a FZ puller. Numerical simulations show

* Corresponding author. Tel.: +371 67033796.
E-mail address: andrejs.sabanskis@lu.lv (A. Sabanskis).

http://dx.doi.org/10.1016/j.jcrysgro.2014.07.041
0022-0248/© 2014 Elsevier B.V. All rights reserved.

that q_{gas} is much smaller than q_{rad} and can be neglected, however, the shear stress of gas flow can noticeably influence melt flow pattern and crystallization interface deflection.

2. Mathematical model and calculation algorithm

2.1. Model of gas flow

Due to large temperature variations in a FZ Si puller, gas density varies by a factor of 4. Because of this, the Boussinesq approximation cannot be used and compressible flow in a low Mach number approximation is considered, since gas flow velocity is much smaller than the speed of sound.

The ideal gas law (2) is used to describe the gas density, ρ, dependence on the absolute temperature, T. In the equation, p is the pressure, M_g is the molar mass of gas and R is the universal gas constant:

$$\rho = p\frac{M_g}{RT} \tag{2}$$

For the temperature dependence of dynamic viscosity, μ, Sutherland's law (3) is used. The values of gas-specific constants A_S and T_S are given in Table 1. The dependence of μ on pressure is neglected as the main contribution of viscosity change is the large variations of temperature:

$$\mu(T) = \frac{A_S\sqrt{T}}{1+T_S/T} \tag{3}$$

The governing equations for steady-state gas flow are continuity equation (4) and Navier–Stokes equations (5):

$$\nabla(\rho\vec{U}) = 0 \tag{4}$$

$$\nabla(\rho\vec{U}\otimes\vec{U} + \tfrac{2}{3}\mu_{\text{eff}}\nabla\vec{U} - 2\mu_{\text{eff}}e) = -\nabla p_{\text{rgh}} - \vec{g}\,\vec{x}\,\nabla\rho \tag{5}$$

In OpenFOAM [10], which is software of choice for gas flow calculations, $p_{\text{rgh}} = p - \rho\vec{g}\,\vec{x}$. In the equations above, $\vec{U}$ is the gas velocity, $\vec{g}$ is the gravity vector, $\vec{x}$ is the spatial position vector, $e = (\nabla\vec{U} + \nabla\vec{U}^T)/2$ is the strain rate tensor, $\mu_{\text{eff}} = \mu + \mu_t$, and μ_t is the turbulent viscosity obtained from a turbulence model.

For velocity, the no-slip boundary condition is applied at solid walls. Crystal pulling and rotation is neglected since the corresponding velocities are much lower than typical gas flow velocity of 1 m/s. For axisymmetric calculations in OpenFOAM, the *wedge* boundary condition is applied at front and back planes of the one cell thick computational domain.

For the modeling of turbulence, the SST k-omega turbulence model for compressible fluid (with default model coefficients) is used, which is provided by OpenFOAM. For the sake of brevity, the model equations are not repeated here, since they are readily available in textbooks, such as Ref. [11].

The energy transfer in the system is described by the enthalpy equation (6), where $\tilde{h} = c_p T$ is the specific enthalpy and c_p is the specific heat capacity at constant pressure, which is assumed to be constant. $\alpha = \mu/\text{Pr}$ is thermal diffusivity for enthalpy, Pr is the Prandtl number. Similarly as in the case of turbulent viscosity, α_t is calculated by a turbulence model:

$$\rho\vec{U}\nabla\left(\tilde{h} + \frac{U^2}{2}\right) = \nabla(\alpha_{\text{eff}}\nabla h), \quad \alpha_{\text{eff}} = \alpha + \alpha_t \tag{6}$$

For the temperature field (calculated from enthalpy) the first-type boundary condition is applied at solid walls.

The relevant parameter values for argon and helium are summarized in Table 1. It is worth pointing out that thermal conductivity and kinematic viscosity of helium are about 8 times higher than that of argon, therefore several times stronger cooling by helium is expected.

Table 1
Physical properties of argon and helium [14,15].

Parameter	Argon	Helium	Unit
M_g	39.948	4.0026	g mol^{-1}
c_p	520	5193	J kg^{-1} K^{-1}
A_S	2.130	1.811	μPa s K$^{-1/2}$
T_S	199.2	205.3	K
Pr	0.67	0.67	–

2.2. Overall calculation algorithm

For the axisymmetric calculations of silicon phase boundaries and flow in molten silicon a specialized program FZone is used [7]. Calculations of gas flow in a FZ puller are carried out using an open source software package OpenFOAM. The calculation procedure for investigating the influence of gas flow is as follows:

1. Calculation of the quasi-stationary shape of phase boundaries and melt HD using FZone.
2. Creation of the geometry for gas flow calculations and automatic finite volume mesh generation.
3. Interpolation of the temperature field on the silicon surfaces of the generated finite volume mesh.
4. Calculation of the axisymmetric steady-state gas flow using OpenFOAM standard solver buoyantSimpleFoam.
5. Calculation of the quasi-stationary shape of phase boundaries and melt HD with gas cooling (q_{gas}) taken into account using FZone.

The gas cooling is considered as described by Eq. (1), $q_{loss} = q_{rad} + q_{gas}$, where q_{gas} is obtained directly from gas flow calculations. In principle, gas cooling influences temperature distribution in Si, which, in its turn, affects gas flow and q_{gas}, therefore, steps 2–5 should be repeated until q_{gas} and temperature at Si boundaries are converged. However, calculations show that the temperature change between steps 1 and 5 is relatively small (by less than 0.6% at free melt surface and 19% at the bottom part of the crystal, where q_{rad} is 20 times smaller than that at the ETP), therefore a single global iteration is considered (steps 1–5).

3. Results and discussion

3.1. System description

The 4 in FZ system from Leibniz Institute for Crystal Growth was considered [12]. Crystal radius was 51 mm, feed rod radius 49 mm, crystal pull rate 3.4 mm/min, inductor current frequency 3 MHz, crystal rotation rate 6 rpm, feed rod rotation rate 0.8 rpm. Length of cylindrical part of crystal and feed rod was set to 24 cm and 32 cm, correspondingly.

Inductor current was adjusted during the calculations with FZone to ensure target zone height of 34.87 mm.

3.2. Melt convection and phase boundaries

The physical properties of silicon from Ref. [7] are used. Since the Marangoni coefficient, M, is not known precisely as it depends on oxygen partial pressure in a puller [13], calculations with different values of M were carried out. Three typical values were chosen: $M = -0.13$, -0.16 and -0.25 mN m^{-1} K^{-1}. Calculation results – inductor current, I, crystallization interface deflection,

H_C, and maximum melt temperature, T_{max}^{melt} – are summarized in Table 2.

A fragment of used finite element mesh in silicon domains in the vicinity of inductor is shown in Fig. 1. The total number of elements in the melt is 6746 in the crystal – 771 and in the feed rod – 784.

The calculated meridional velocity and temperature fields of the non-stationary melt flow in representative time moments for the considered cases are depicted in Fig. 2. For smaller values of $|M|$ the melt flow is more intense and temperature in melt is higher. Standard deviation of the maximum temperature in melt decreases with the increase of $|M|$.

For a detailed analysis, the time-averaged electromagnetic and Marangoni surface forces (f_{EM} and f_{Ma}, correspondingly) at the free melt surface are shown in Fig. 3. The force is positive when it is directed towards the external triple point (ETP). $|f_{EM}|$ decreases with the increase of $|M|$, which is caused by the decrease of inductor current (Table 2) and increase of distance between free surface and inductor (Fig. 4) as a result of maintaining equal zone height for all cases. The change of EM force is localized in the vicinity of the neck region and ETP, while no noticeable changes occur in the central part of the free melt surface. $|f_{Ma}|$, on its turn,

Table 2
Summary of inductor current, I, crystallization interface deflection, H_C, and maximum melt temperature, T_{max}^{melt}, for the considered cases.

M (mN m^{-1} K^{-1})	Cooling	I (A)	H_C (mm)	T_{max}^{melt} (K)
−0.13	None	941 ± 11	15.1 ± 0.5	1708 ± 3
−0.16	None	934 ± 7	13.9 ± 0.4	1708 ± 2
−0.16	Argon	968 ± 3	12.8 ± 0.2	1711 ± 2
−0.16	Helium	1087 ± 1	11.5 ± 0.1	1714 ± 2
−0.25	None	917.3 ± 0.3	10.93 ± 0.03	1705.9 ± 0.4
−0.25	Argon	950.4 ± 0.2	10.27 ± 0.01	1708.6 ± 0.2
−0.25	Helium	1064.4 ± 0.3	10.07 ± 0.02	1714 ± 1

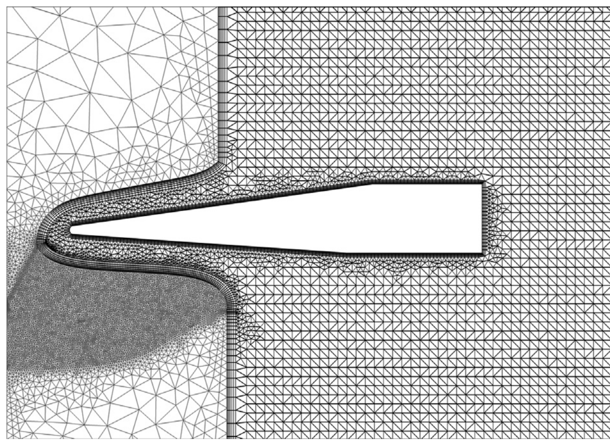

Fig. 1. Finite element mesh in silicon and finite volume mesh in gas in the vicinity of inductor.

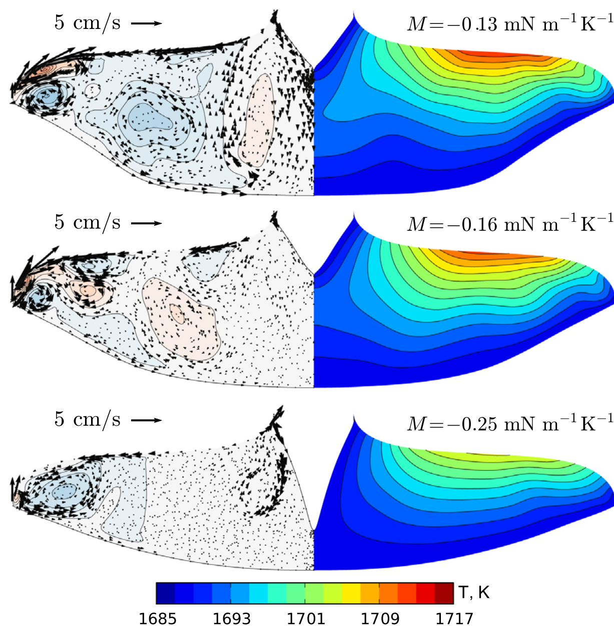

Fig. 2. Instantaneous meridional velocity and stream function (red – clockwise, blue – anti-clockwise vortices) fields (left) and temperature distribution (right) in melt for cases with different Marangoni coefficients. No gas cooling is applied. (For interpretation of the references to color in this figure caption, the reader is referred to the web version of this paper.)

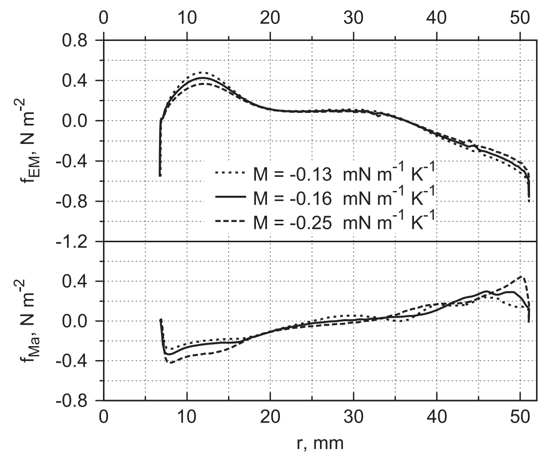

Fig. 3. Electromagnetic force (top) and Marangoni force (bottom) as a function of radial coordinate, r, for cases with different Marangoni coefficients. No gas cooling is applied.

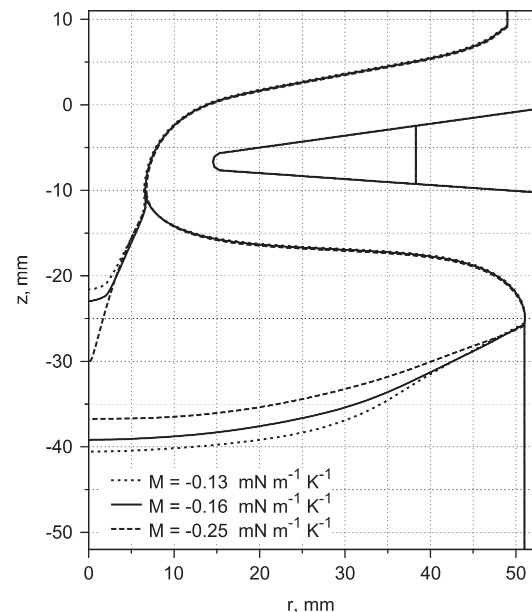

Fig. 4. Shape of phase boundaries for cases with different Marangoni coefficients. No gas cooling is applied.

increases with $|M|$, and these changes take place roughly in the same regions as change of $|f_{EM}|$.

f_{EM} and f_{Ma} typically act in opposite directions, and the interaction between these forces influences flow pattern and temperature field in the melt. However, f_{Ma} cannot be analyzed separately because it depends on the resulting melt temperature.

For small $|M|$ the EM force dominates over the Marangoni force, producing strong flow towards the center of the free melt surface (Fig. 2, top). With the increase of $|M|$ to 0.16 mN m^{-1} K^{-1} the difference between $|f_{EM}|$ and $|f_{Ma}|$ decreases, but EM force still dominates, producing similar flow pattern as before (Fig. 2, middle). For even larger $|M| = 0.25$ mN m^{-1} K^{-1} when neither f_{EM} nor f_{Ma} is dominating, the flow regime is completely different (Fig. 2, bottom). The flow steadiness increases with $|M|$, which is clearly visible from the deviations of variables in Table 2 from their average values.

Because of melt HD, the quasi-stationary shapes of phase boundaries also depend on the Marangoni coefficient, see Fig. 4. The largest differences have the shapes of the crystallization and melting interfaces. Melt flow affects temperature field at the ETP and causes vertical movement of ETP. For higher currents (i.e., smaller $|M|$) the open melting front and free melt surfaces shift upwards to maintain the predefined zone height. The melting interface shifts upwards locally near the symmetry axis due to larger EM heat sources and altered melt HD.

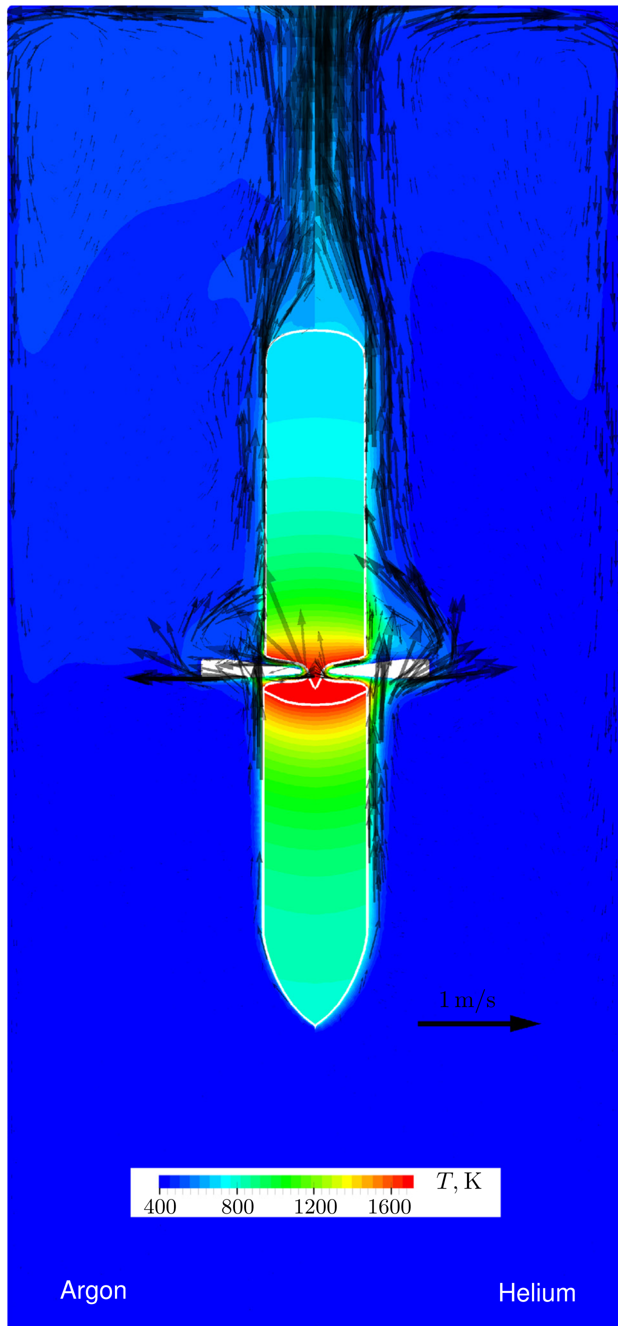

Fig. 5. Global view of gas temperature and velocity fields (left – argon, right – helium). Also shown are the temperature field in Si domains and the shape of Si phase boundaries (white).

3.3. Gas flow

Gas flow in a FZ puller is calculated for argon and helium. Although argon is typically used in FZ Si growth, helium is also considered to investigate the effects of stronger cooling.

A fragment of the generated finite volume mesh consisting of ca. 73 000 cells is shown in Fig. 1. For a higher accuracy, boundary layers are used at solid walls. Puller height is chosen to be 1.3 m and radius – 0.3 m. Temperature of inductor and puller walls is set to 400 K.

A global view of calculated temperature and velocity fields in argon and helium is shown in Fig. 5, and an example of gas flow in the vicinity of the inductor – in Fig. 6. The gas flow is directed downwards along vertical puller wall, and upwards along hot Si surfaces. At the inductor, the flow splits into two parts: (i) flow

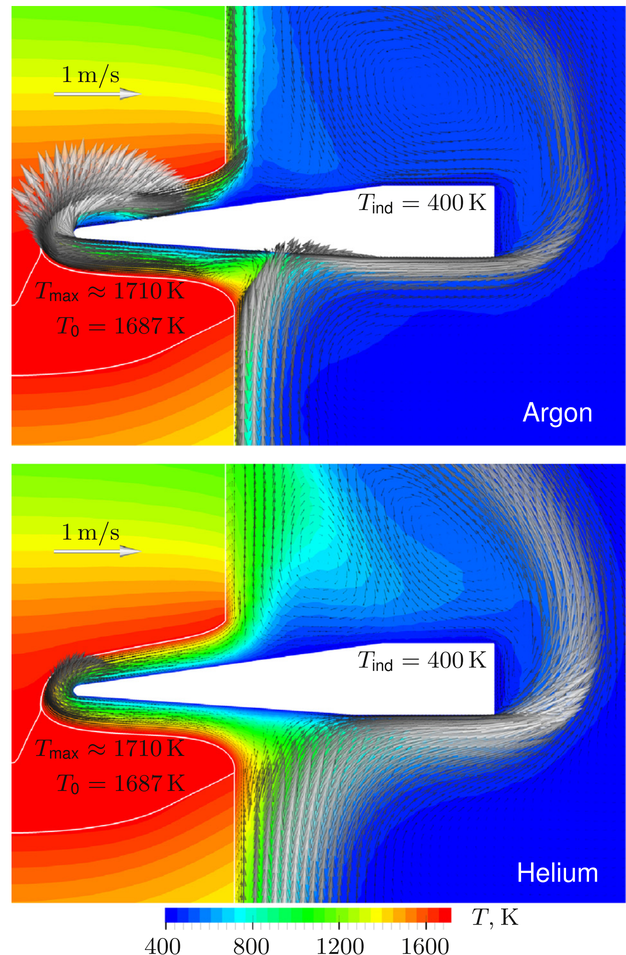

Fig. 6. Gas temperature and velocity fields in the vicinity of the inductor (top – argon, bottom – helium). Also shown are the temperature field in Si domains and shape of Si phase boundaries (white).

around the outer part of inductor and (ii) flow along the free melt surface and open melting front. The characteristic maximum velocity is around 1 m/s for both gases. Maximal temperature at the free surface is $T_{max} \approx 1710$ K, 23 K above melting point of silicon, $T_0 = 1687$ K. The boundary layer thickness of temperature and velocity fields is larger for helium due to its higher thermal diffusivity and kinematic viscosity. The gas flow along the free melt surface is weaker for helium due to a thicker velocity boundary layer at the crystal surface, resulting in smaller gas shear stress, f_{gas}, which is depicted in Fig. 7. For argon flow, a small vortex exists near the ETP, which reverses the direction of f_{gas} locally.

Fig. 8 gives an overview of the cooling strength of gas flow. For argon, the ratio q_{gas}/q_{rad} varies from 5% to 30%, while for helium it is 10–80% and even higher. The high values of q_{gas}/q_{rad} occur at the end of the crystals (not shown in Fig. 8), where q_{rad} is small. A non-negligible gas cooling takes place also at the free melt surface and open melting front, as well as at feed rod surface, which was not considered by other researchers in Refs. [5,3].

Gas temperature in a puller away from the hot zone is close to 400 K, which corresponds to the defined puller wall temperature. A slightly higher average gas temperature of 490 K was measured by Menzel [3]. The value of $T_g = 400$ K was used to estimate the heat transfer coefficient, which is plotted on the right panel of Fig. 8. Typical value of h for the cooling of crystal by argon is around 9 W m^{-2} K^{-1}, for helium it reaches 29 W m^{-2} K^{-1}. The heat transfer coefficient for argon is in a good agreement with literature data [5,3], while no data are available for FZ Si growth in helium atmosphere. The cooling of the feed rod is not as strong: $h \approx 4$ W m^{-2} K^{-1} for argon and 10 W m^{-2} K^{-1} for helium.

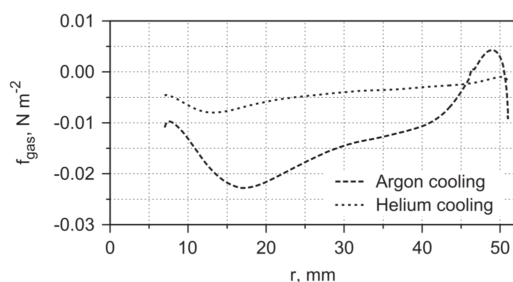

Fig. 7. Gas shear stress as a function of radial coordinate, r.

3.4. Influence of gas flow on melt convection and phase boundaries

The calculated argon and helium cooling heat flux density q_{gas} (left panel of Fig. 8) is taken into account for melt HD and phase boundary calculations with FZone. The influence of gas shear stress (Fig. 7) is neglected in the present study since it is an order of magnitude weaker than EM and Marangoni forces and will only have a noticeable influence when f_{EM} almost completely compensates f_{Ma}.

Two values or Marangoni coefficient is considered: $M = -0.16$ and -0.25 mN m^{-1} K^{-1}. In all the cases, the inductor current was increased to compensate additional heat losses by the larger induced heat sources and to ensure target zone height. The main results are summarized in Table 2.

3.4.1. $M = -0.16$ mN m^{-1} K^{-1}

The calculated instantaneous meridional velocity and temperature fields in melt for cases with argon and helium cooling are depicted in Fig. 9. For argon cooling the melt HD is practically unchanged (compare with Fig. 2, middle), while for helium cooling melt flow is clearly more intense.

The time-averaged f_{EM} and f_{Ma} distributions are presented in Fig. 10. For argon cooling $|f_{EM}|$ increases locally by ca. 10%, while for helium cooling the increase is by 74%, compared to the case without cooling. $|f_{EM}|$ increases due to two factors: the increase of inductor current (Table 2) and the decrease of distance between free surface and inductor (Fig. 11). $|f_{Ma}|$ remains effectively unchanged for all the cases because the flow is already in the regime of dominating EM force and for stronger cooling $|f_{EM}|$ increases more rapidly than $|f_{Ma}|$ and prevents larger temperature gradients along free surface.

In Fig. 11 the shapes of phase boundaries are depicted. Argon cooling decreases crystallization interface deflection by 8% while

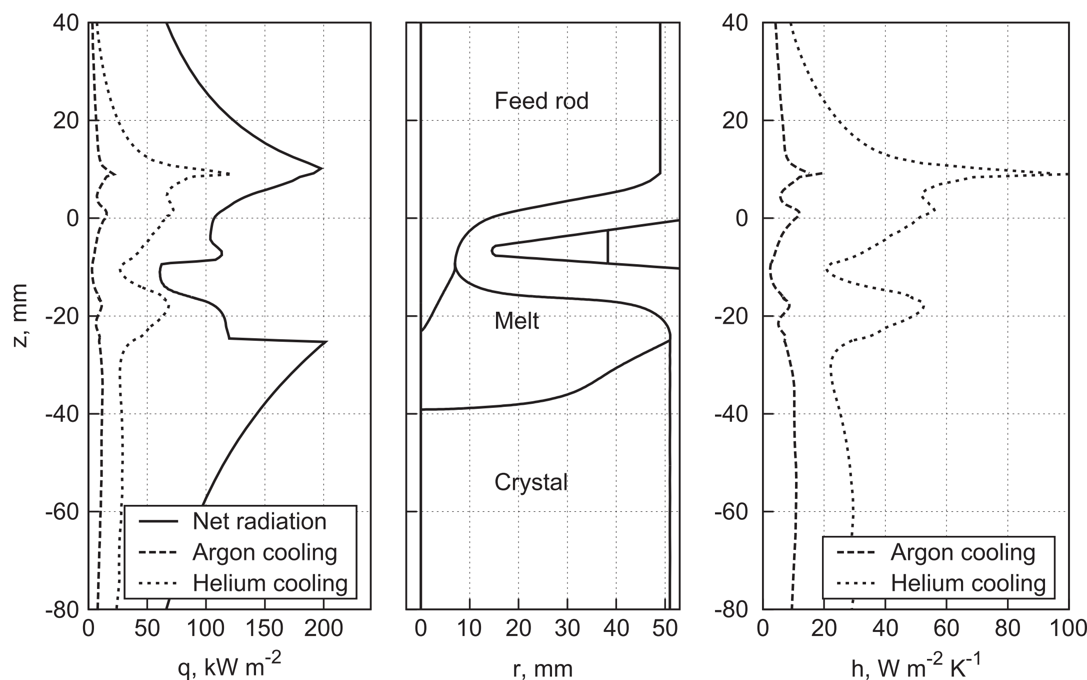

Fig. 8. Left: gas cooling heat flux densities, compared to net radiation heat losses. Center: shape of Si boundaries for a reference of the vertical coordinate, z. Right: heat transfer coefficient.

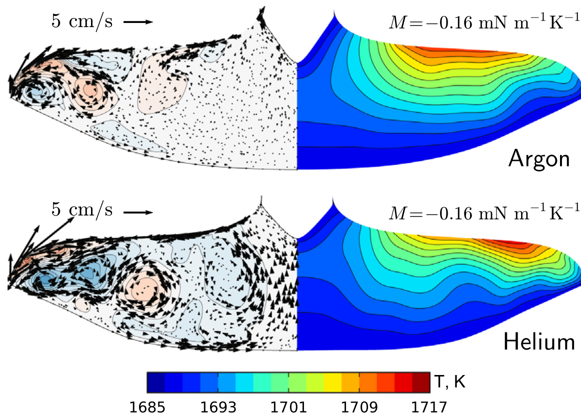

Fig. 9. Instantaneous meridional velocity and stream function (red – clockwise, blue – anti-clockwise vortices) fields (left) and temperature distribution (right) in melt for $M = -0.16\ \mathrm{mN\ m^{-1}\ K^{-1}}$. (For interpretation of the references to color in this figure caption, the reader is referred to the web version of this paper.)

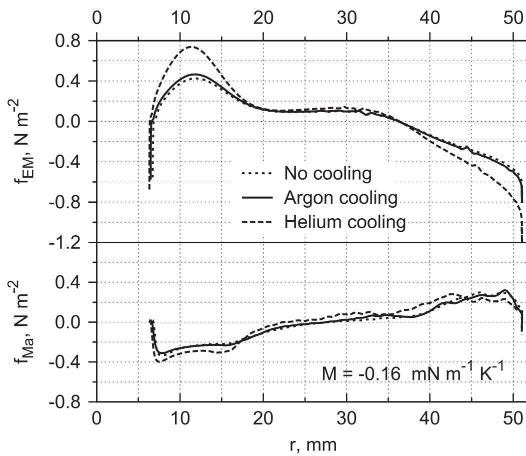

Fig. 10. Electromagnetic force (top) and Marangoni force (bottom) as a function of radial coordinate, r. $M = -0.16\ \mathrm{mN\ m^{-1}\ K^{-1}}$.

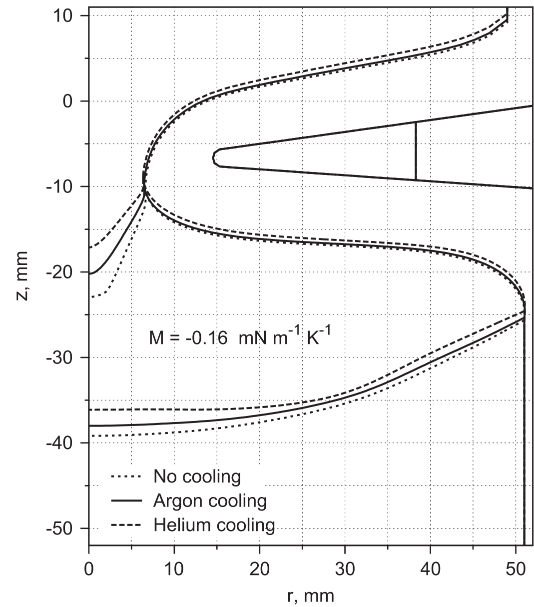

Fig. 11. Shape of phase boundaries for $M = -0.16\ \mathrm{mN\ m^{-1}\ K^{-1}}$.

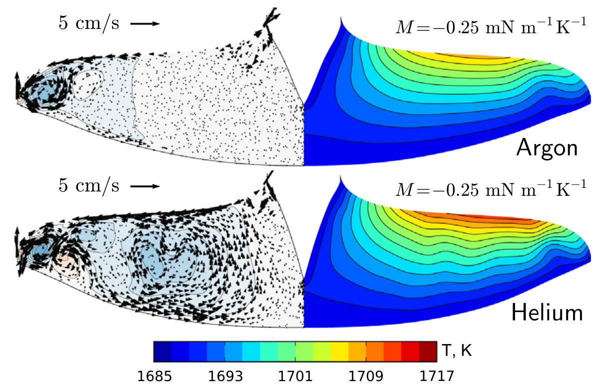

Fig. 12. Instantaneous meridional velocity and stream function (red – clockwise, blue – anti-clockwise vortices) fields (left) and temperature distribution (right) in melt for $M = -0.25\ \mathrm{mN\ m^{-1}\ K^{-1}}$. (For interpretation of the references to color in this figure caption, the reader is referred to the web version of this paper.)

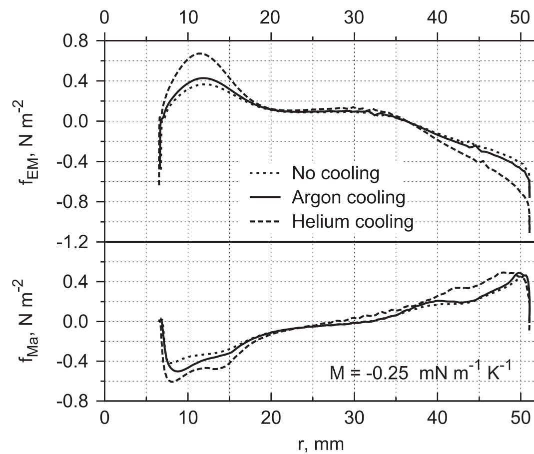

Fig. 13. Electromagnetic force (top) and Marangoni force (bottom) as a function of radial coordinate, r. $M = -0.25\ \mathrm{mN\ m^{-1}\ K^{-1}}$.

preserving its shape, but helium cooling decreases deflection by 17% and deforms the shape of the crystallization interface. The decrease of deflection for stronger cooling is also reported in Refs. [3,5]. For higher currents (i.e., larger q_{gas}) due to changes in melt HD the open melting front and free melt surfaces shift upwards as discussed in Section 3.2. The melting interface shifts upwards due to larger EM heat sources and altered melt HD.

3.4.2. $M = -0.25\ \mathrm{mN\ m^{-1}\ K^{-1}}$

The calculated instantaneous meridional velocity and temperature fields for argon and helium cooling are depicted in Fig. 12. As it was observed in Section 3.4.1, the melt HD is practically unchanged for argon cooling (compare with Fig. 2, bottom), while for helium cooling melt flow is more intense.

The time-averaged f_{EM} and f_{Ma} distributions are presented in Fig. 13. For EM force the results are similar to those reported in Section 3.4.1: for argon cooling $|f_{EM}|$ increases by 17%, for helium – by 83%. However, different results are obtained for the Marangoni force: argon cooling causes only a slight increase of $|f_{Ma}|$, while helium cooling increases $|f_{Ma}|$ locally by a factor of 1.5…2. This effect is caused by the flow regime: for the cases without cooling and with argon cooling neither f_{EM} nor f_{Ma} is dominating. For helium cooling $|f_{EM}|$ and EM heat sources become substantially larger and increase temperature in melt, resulting in the increase of $|f_{Ma}|$.

In Fig. 14 the shapes of phase boundaries are depicted. Both argon and helium cooling have a weak influence on the crystallization interface deflection, decreasing it by 6% and 8%,

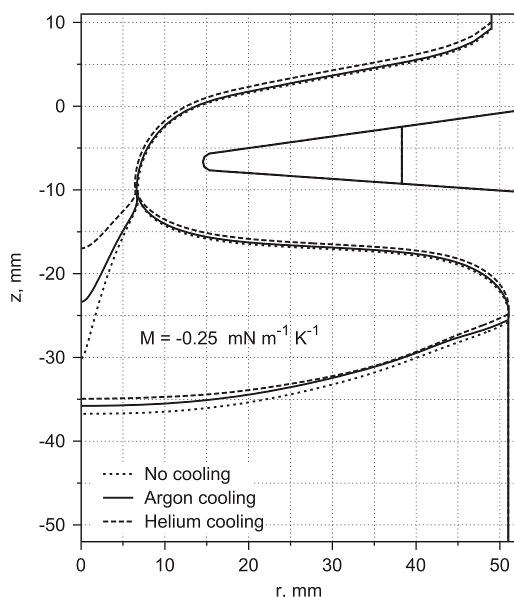

Fig. 14. Shape of phase boundaries for $M=-0.25\ \mathrm{mN\,m^{-1}\,K^{-1}}$.

correspondingly. As in Section 3.4.1, the decrease of deflection for stronger cooling agrees qualitatively with literature data [5,3]. With the increase of cooling strength the open melting front and free melt surfaces move upwards as described in Sections 3.2 and 3.4.1. The melting interface shifts upwards due to larger EM heat sources and altered melt HD.

4. Conclusions

Axisymmetric calculations of argon and helium flow in FZ system have been carried out using OpenFOAM software. In contrast to other works in which only the crystal cooling is considered, the present model allows us to predict the distribution of cooling heat flux densities at crystal, feed rod, open melting front and free melt surfaces. A specialized program FZone was used to model the influence of gas cooling on melt flow and shape of phase boundaries. It is found that argon cooling power density is 5–30% of net radiation heat flux density, for helium it reaches 10–80%. The heat transfer coefficient for crystal is around $9\ \mathrm{W\,m^{-2}\,K^{-1}}$ for argon and $29\ \mathrm{W\,m^{-2}\,K^{-1}}$ for helium and is in a good agreement with simpler models [5,3].

For stronger gas cooling larger inductor current is required to compensate the increased heat losses, which produces larger EM force. The interplay between EM and Marangoni forces, which determines the melt flow regime, was analyzed for different values of Marangoni coefficient and different cooling gases. It is found that by increasing EM force (e.g., by changing current due to stronger cooling), flow regime can change from non-intense, with smooth temperature isolines, to a more intense and non-stationary flow. Generally, EM force increases with the cooling strength but the change of Marangoni force depends on the flow regime.

The crystallization interface deflection decreases for stronger cooling, which agrees qualitatively with available literature data [5,3]. For $M=-0.16\ \mathrm{mN\,m^{-1}\,K^{-1}}$ the decrease is by 8% for argon and by 17% for helium cooling, while for $M=-0.25\ \mathrm{mN\,m^{-1}\,K^{-1}}$ the decrease is by 6% (argon) and 8% (helium) due to a less intense melt flow.

Shear stress of gas flow is by an order of magnitude weaker than EM and Marangoni forces and is expected to have only a minor influence on the melt flow and interface shapes.

Acknowledgments

The present work is carried out at the University of Latvia and has been supported by the European Regional Development Fund, project Contract no. 2013/0051/2DP/2.1.1.1.0/13/APIA/VIAA/009.

References

[1] W. Zulehner, Historical overview of silicon crystal pulling development, Mater. Sci. Eng. B: Solid-State Mater. Adv. Technol. 73 (2000) 7–15.
[2] T. Duffar (Ed.), Crystal Growth Processes Based on Capillarity, John Wiley & Sons, Ltd, Chichester, 2010.
[3] R. Menzel, Growth conditions for large diameter FZ Si single crystals (Ph.D. thesis), Technischen Universität Berlin, 2013.
[4] A. Mühlbauer, A. Muiznieks, J. Virbulis, A. Lüdge, H. Riemann, Interface shape, heat transfer and fluid flow in the floating zone growth of large silicon crystals with the needle-eye technique, J. Cryst. Growth 151 (1995) 66–79.
[5] T.L. Larsen, Phosphorus diffusion in float zone silicon crystal growth (Ph.D. thesis), Technical University of Denmark, 2000.
[6] F. Bioul, Use of mathematical expansions to model crystal growth from the melt under the effect of magnetic fields (Ph.D. thesis), Université catholique de Louvain, 2007.
[7] G. Ratnieks, Modelling of the floating zone growth of silicon single crystals with diameter up to 8 inch (Ph.D. thesis), University of Latvia, Rīga, 2007.
[8] M. Wünscher, Crucible-free crystal growth of germanium—experiments and simulations (Ph.D. thesis), Technischen Universität Berlin, 2011.
[9] V. Kalaev, I. Evstratov, Y. Makarov, Gas flow effect on global heat transport and melt convection in Czochralski silicon growth, J. Cryst. Growth 249 (2003) 87–99.
[10] The open source CFD toolbox OpenFOAM, June 11, 2014, 〈http://www.openfoam.org/〉.
[11] T. Cebeci, Turbulence Models and Their Application: Efficient Numerical Methods With Computer Programs, Horizons Publishing, Inc, Long Beach; Springer-Verlag, Berlin, Heidelberg, New York, 2004 (jointly published).
[12] H.-J. Rost, R. Menzel, A. Luedge, H. Riemann, Float-zone silicon crystal growth at reduced RF frequencies, J. Cryst. Growth 360 (2012) 43–46 (The 5th International Workshop on Crystal Growth Technology).
[13] Z.F. Yuan, K. Mukai, W.L. Huang, Surface tension and its temperature coefficient of molten silicon at different oxygen potentials, Langmuir 18 (2002) 2054–2062.
[14] D.R. Lide (Ed.), CRC Handbook of Chemistry and Physics, CRC Press, Boca Raton, FL, 2003.
[15] E. Bich, J. Millat, E. Vogel, The viscosity and thermal conductivity of pure monatomic gases from their normal boiling point up to 5000 K in the limit of zero density and at 0.101325 MPa, J. Phys. Chem. Ref. data 19 (1990) 1289–1305.

International Scientific Colloquium
Modelling for Electromagnetic Processing
Hannover, September 16-19, 2014

Modelling of dopant transport during floating zone growth of silicon

A. Sabanskis, K. Surovovs, A. Krauze, J. Virbulis

Abstract

The floating zone (FZ) silicon single crystal growth process is modelled, considering non-stationary melt velocity, temperature, pressure and dopant concentration fields. Due to the high purity of the obtained crystal, modelling of dopant transport is carried out more carefully: new boundary conditions for dopant concentration in the melt are obtained from gas flow simulations. Radial resistivity profiles of the crystal, calculated from the modelled concentration field, are compared with experimental data from the Institute of Crystal Growth, Berlin.

1. Introduction

Nowadays, silicon single crystals are very important in semiconductor electronics. By doping Si crystals with boron or phosphorus, different values of conductivity can be obtained due to electrons or electron holes. Crystal resistivity strongly depends on the concentration of charge carriers, which is almost equal to the concentration of dopants.

For power electronics, FZ grown crystals are used due to high purity, because the melt has no contact with any other system part. In this process, a polycrystalline silicon feed rod is melted using a high-frequency (HF) electromagnetic (EM) field generated by an induction coil, then the melt flows downwards and cools down due to heat radiation. Then it is touched by the seed crystal, which is then pulled down, adjusting the pulling velocity to ensure cylindrical growth of the single crystal. When the radius of the feed rod is much greater than the radius of the hole in the inductor, it is called “needle-eye” technique.

Although the FZ needle-eye technique is known for many years, innovations are needed to improve performance and reduce the cost/quality ratio of the process. Crystal growth companies want to get as good crystals as possible – with homogeneous distribution of crystal resistivity and without dislocations. Real experiments are time-consuming and expensive, so numerical simulations are widely applied to support the development of FZ systems.

Developed software allows modelling the FZ process in detail, including the 3D hydrodynamics in liquid silicon and gas flow in the FZ puller. Therefore, it is very important to investigate, which boundary conditions (BC) should be used for dopant concentration to obtain the most correct description of a real system and the best correspondence with experiment. In this work, new BC for dopant transport calculations in the melt are derived from gas flow calculations. Most frequently dopants are brought into the melt by spraying them into the atmosphere of the puller near the free surface of the molten zone. This input method was simulated in gas flow calculations to obtain dopant concentration flow through the free surface and then use the results as a BC for dopant transport in the melt. From the non-stationary concentration field, the radial resistivity variation (RRV) profiles in the grown single crystal are obtained, then azimuthally averaged and averaged in time. To analyze the

influence of the new BC, resistivity distribution in the crystal is compared with experimental data from the Institute of Crystal Growth (ICG), Berlin, obtained by H.-J. Rost et. al. [1].

2. Mathematical models

2.1. Phase boundaries

The stationary state of phase boundaries was obtained in the previously developed program *FZone* using an axially symmetrical approximation [2]. It was found iteratively by moving elements of interfaces with velocities that correspond to heat fluxes. The open melting front is calculated using a thin film model that takes into account gravity, viscosity and mass inflow from the feed rod melting due to EM heat sources. The inductor is strongly non-symmetrical, therefore the HF EM field is calculated in 3D and then azimuthally averaged to get heat sources for boundary conditions for the temperature calculations [3]. Melt motion was not taken into account.

2.2. Gas flow

Quasi-stationary buoyancy-driven gas flow in the system with fixed boundaries (pulling and rotation of silicon is not taken into account due to the relatively small velocity) is calculated using a SST k-ω low-Re turbulence model. Due to strong temperature dependence, gas density was calculated using the ideal gas law, viscosity – using Sutherland's law. An axially symmetrical approximation is used because of the big mesh size (1.3 x 0.3 meters, ca. 73000 cells). Equations solved by the solver *buoyantSimpleFoam* from the open source library *OpenFOAM* are shown below:

$$\nabla(\rho\vec{U}) = 0, \tag{2.1}$$

$$\nabla(\rho\vec{U}\vec{U}) = -\nabla\left(p - \rho\vec{g}\vec{x} + \frac{2}{3}\mu_{\text{eff}}\nabla\vec{U}\right) - \vec{g}\vec{x}\nabla\rho + \nabla[\mu_{\text{eff}}(\nabla\vec{U} + \nabla\vec{U}^T)], \tag{2.2}$$

$$(\rho\vec{U})\nabla h - \nabla(\alpha_{\text{eff}}\nabla h) = \vec{U}\nabla p, \qquad \alpha_{\text{eff}} = \alpha + \alpha_t\,, \tag{2.3}$$

$$(\rho\vec{U})\nabla C = \nabla(\rho D_{\text{eff}}\nabla C), \qquad D_{\text{eff}} = \frac{\nu}{\text{Sc}} + \frac{\nu_t}{\text{Sc}_t}\,, \tag{2.4}$$

where $\vec{U}$ is melt velocity, ρ – density, p – pressure, $\vec{x}$ – radius vector, $\mu_{\text{eff}} = \mu + \mu_t$ – effective viscosity of argon (the sum of molecular and turbulent), $\vec{g}$ – gravity vector, $h = c_pT$ – enthalpy, α – diffusion coefficient of enthalpy, C – dopant concentration, Sc – Schmidt number and D – diffusion coefficient for the concentration. In Tab. 1 all BC are shown.

Tab. 1. Boundary conditions for gas flow calculations

Boundary	$\vec{U}$	T	C
Inlet	$\vec{U} = V = const$, V is dopant inlet velocity	$\frac{\partial T}{\partial n} = 0$	$C = 1$
Surface of solid silicon	no slip	T distribution from *FZone*	$\frac{\partial C}{\partial n} = 0$
Surface of liquid silicon	no slip	T distribution from *FZone*	$C = 0$
Walls of puller, inductor, outlet	no slip, outlet	$T = 1687$ K	$\frac{\partial C}{\partial n} = 0$

2.3. 3D melt flow

3D unsteady calculations of melt hydrodynamics are carried out with the previously developed laminar solver *FZSiFOAM*, based on the open source library *OpenFOAM*. Non-symmetrical heat sources and EM forces are taken into account solving equations for melt

velocity, temperature, pressure and dopant concentration. Only the main modification is mentioned in this section, for details see [4,5].

Different BC for the dopant concentration C are used (see Fig. 1): either constant concentration C_{free} or the distribution of the concentration gradient $\frac{\partial C_{\mathrm{free}}}{\partial n} = j_{\mathrm{fs}}$ on the melt free surface obtained from the results of gas flow calculations were used. The concentration value on the ring-shaped profile [5] was adjusted depending on the C inflow through theopen melting front j_{of}:

$$\iint_{S_{\mathrm{of}}} j_{\mathrm{of}}\, \mathrm{d}S = v_{\mathrm{ring}} \pi (R_{ITP}^2 - R_{ring}^2) C_{\mathrm{ring}}\,, \quad (2.5)$$

where S_{of} is the total area of the melting front. The feed rod is assumed to be pure ($C = 0$) and on the crystallization interface a segregation BC is used.

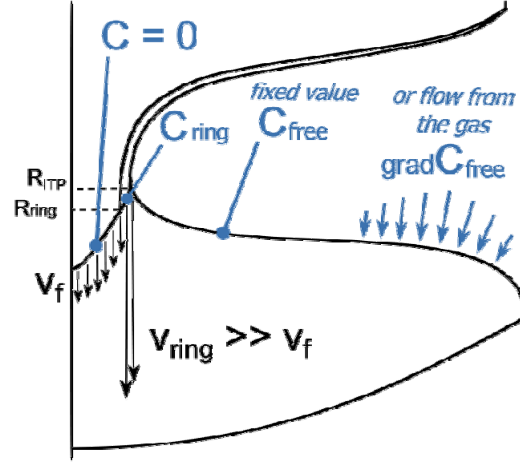

Fig. 1. Boundary conditions for 3D dopant transport calculations.

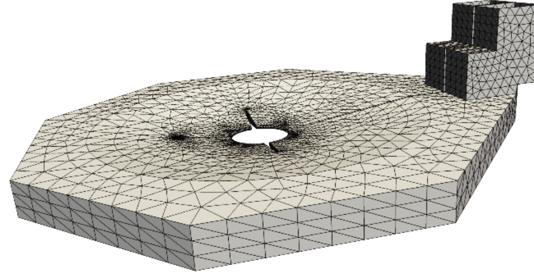

Fig. 5. 3D inductor shape with BEM mesh.

3. Description of the considered system

The 4" FZ system from the Leibnitz Institute for Crystal Growth, Berlin is modelled. It was selected in order to compare RRV with experimental data [1]. Main parameters are shown in Tab. 2 and the 3D inductor shape with a boundary element mesh for HF EM calculations – in Fig. 2.

Tab. 2. Parameters of used FZ system.

Parameter	Value
Zone height	34.87 mm
Crystal pulling rate	3.4 mm/min
Crystal rotation rate	6.0 rpm
Feed rod rotation rate	0.8 rpm
Current frequency	3 MHz

4. Calculation results

4.1. Gas flow

Results of gas flow calculations are shown in Fig. 3. As a result of the gas flow calculations, C distribution, which is necessary for BC for dopant transport in the melt, is summarized in Tab. 3 and Fig. 4. It can be seen that for every value of dopant inlet velocity V, only about 85% of dopants get into the melt through the free surface and thin film on the open melting front. Nevertheless, when V becomes higher, more dopants get into the melt through the free surface (relative to total C inflow).

Tab. 3. Summary of the results of dopant transport calculations in FZ puller atmosphere, for different dopant inlet velocities V. C_{ring} is the value used for boundary conditions on the ring-shaped profile [5], but $\overline{C_{\mathrm{free}}}$ is an average value of C on the free surface, calculated from the results of melt flow calculations with *FZSiFOAM*.

V, m/s	C inflow, a. u.	Through free surface, j_{fs}	Through open front, j_{of}	$j_{\mathrm{fs}}/j_{\mathrm{of}}$	C_{ring}	$\overline{C_{\mathrm{free}}}$
0.0	4.0	57.9%	26.8%	2.16	17.2	22.6
0.1	6.5	58.4%	26.5%	2.20	27.3	35.3
0.3	12.9	59.6%	24.8%	2.40	45.0	62.5
0.5	19.9	60.7%	22.7%	2.68	65.8	91.5

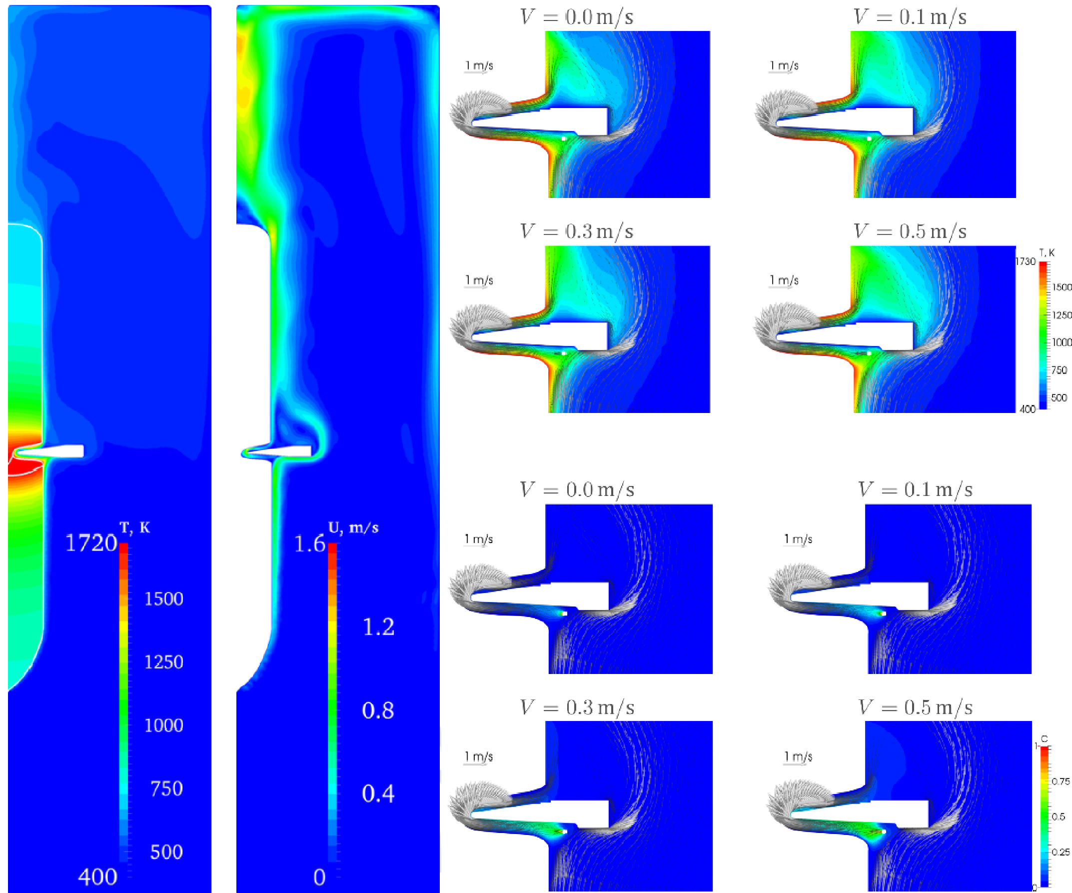

Fig. 3. Left – temperature and gas velocity in the whole FZ system, $V = 0$. Right top – gas velocity vectors and gas temperature in the vicinity of inductor. Right bottom – gas velocity vectors and dopant concentration field in the vicinity of inductor.

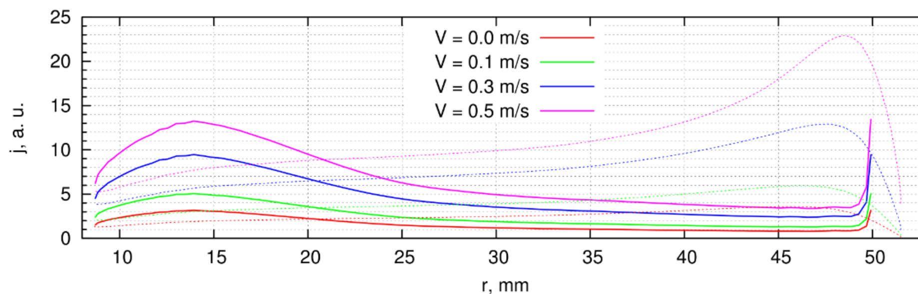

Fig. 4. Radial distribution of the dopant concentration flow through the open melting front (solid) and melt free surface (dashed), in arbitrary units.

4.2. 3D melt flow

To calculate 3D melt flow and dopant transport in the melt, first phase boundaries were calculated by *FZone* using an axially symmetrical approximation. The obtained 2D mesh and temperature field is shown in Fig. 5. Then the shape of the molten zone was rotated around the axis and a 3D finite element mesh with approximately 72 000 elements was created. Melt temperature, velocity and dopant concentration were calculated by *FZSiFOAM* (see Fig. 7, in which typical radial maximum of C can be seen on the crystallization interface, it leads to the minimum in the RRV profile). Fig. 6. shows dopant concentration in the melt for different V, a boundary layer of C is formed at the crystallization interface due to dopant segregation. A closer look at C radial distribution on the melt free surface is given in Fig. 8,

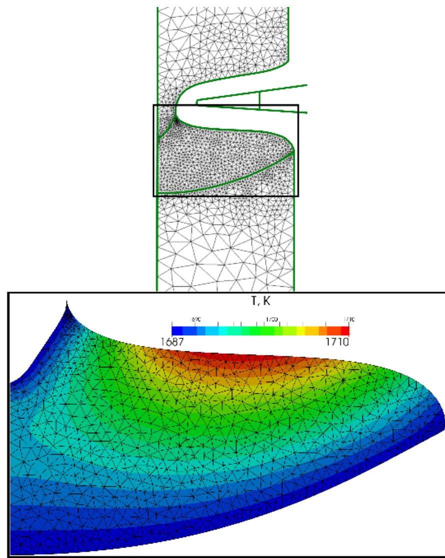

Fig. 5. 2D mesh and temperature field obtained by *FZone*.

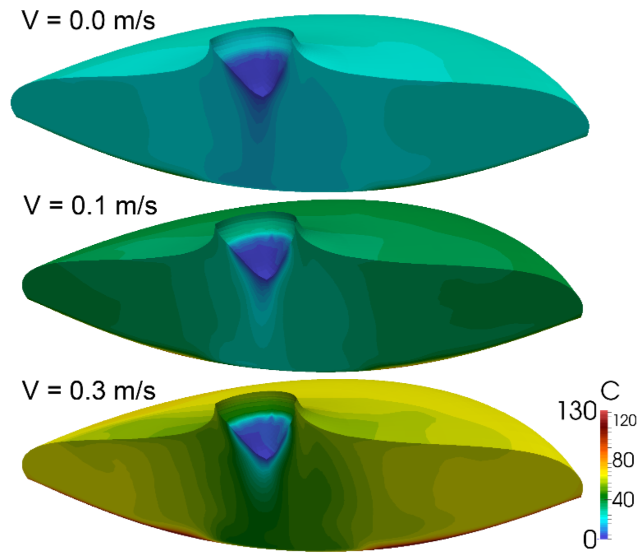

Fig. 6. Dopant concentration distribution (a. u.) in melt for different dopant inlet velocities.

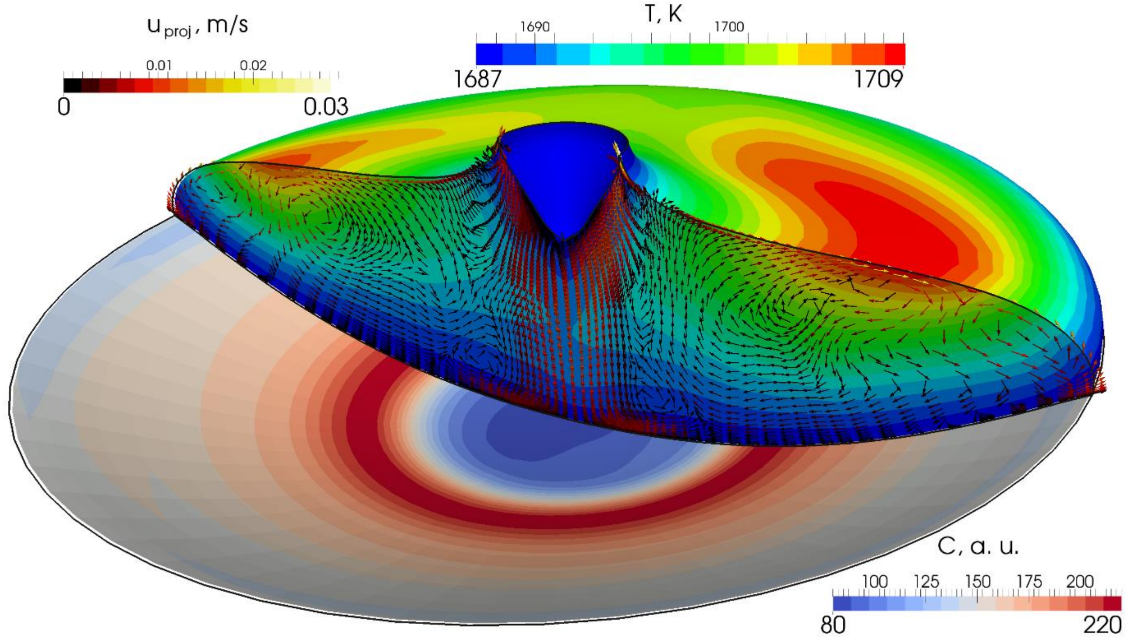

Fig. 7. Time-averaged meridional velocity in the yz plane (⊥ to current suppliers), temperature in melt and dopant concentration on crystallization interface ($V = 0.5$ m/s).

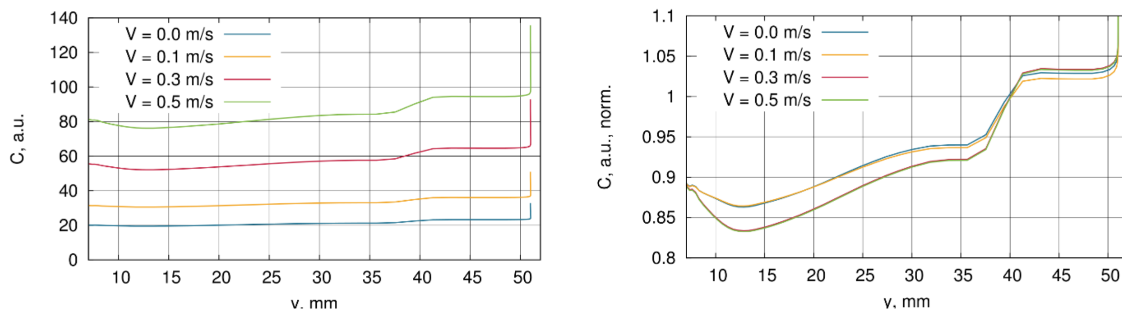

Fig. 8. Radial distribution of time-averaged dopant concentration on melt free surface (in direction ⊥ to current suppliers). Left – absolute values, right – normalised to $\overline{C_{\text{free}}}$.

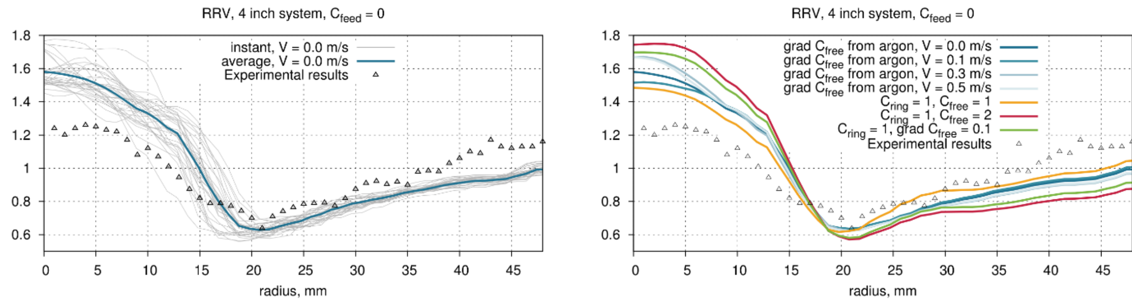

Fig. 9. Left – instantaneous RRV profiles and averaged one (a. u.). Right – averaged RRV profiles for different concentration BC. Experiment from ICG is shown with triangles.

plots show both absolute values and values normalized to $\overline{C_{\text{free}}}$. It can be concluded that the normalized values are rather similar due to intensive mixing of the melt. Finally, RRV profiles are obtained, azimuthally averaged and time-averaged, and normalized for more convenient comparison (see Fig. 9). Variations between cases with different V are small, but these calculations are distinguishable.

Conclusions

New boundary conditions for dopant concentration (C inflow through liquid Si surfaces) were successfully implemented and compared with previously used ones. The influence of dopant inlet velocity V was studied. It was found out that differences in normalized RRV profiles between cases with various dopant inflow rates are small, although absolute values of C in the melt are very different (for V = 0.5 m/s almost five times higher than for V = 0). RRV is mainly affected by the redistribution of integral dopant inflow between the melt free surface and the open melting front, not the C gradient distribution on the free surface. Results for different V are located between previously used Dirichlet BC with fixed C values (1 and 2) on the free surface. Agreement between model and experiment can be improved by back-coupling C from the melt to gas flow simulations or by using 3D non-symmetrical BC for C in the melt.

References

[1] Rost, H.-J.; Menzel, R.; Luedge, A.; Riemann, H.: *FZ silicon crystal growth at reduced RF frequencies*. Journal of Crystal Growth, Vol. 360, 2012, pp. 43-46.

[2] Ratnieks, G.; Muiznieks, A.; Muhlbauer, A.: *Modelling of phase boundaries for large industrial FZ silicon crystal growth with the needle-eye technique*. JCG, Vol. 255, 2003, pp. 227-240.

[3] Muiznieks, A.; Rudevics, A.; Riemann, H.; Lacis, U.: *Comparison between 2D and 3D modelling of HF electromagnetic field in FZ silicon crystal growth process*. Proceedings of the International Scientific Colloquium „Modelling for Material Processing“, Riga, 2010, pp. 61-65.

[4] Rudevics, A.; Lacis, K.; Muiznieks, A.; Jekabsons, N.; Nacke, B.: *Using open source code library OpenFOAM for 3D magneto hydrodynamic calculations in semiconductor crystal growth technologies*. Proceedings of the International Scientific Colloquium „Modelling for Electromagnetic Processing“, 2008, pp. 103-110

[5] Surovovs, K.; Muiznieks, A.; Sabanskis, A.; Virbulis, J.: *Hydrodynamical aspects of the floating zone silicon crystal growth process*. Journal of Crystal Growth, 2014, http://dx.doi.org/10.1016/j.jcrysgro.2013.12.066

Authors

Sabanskis, Andrejs; Surovovs, Kirils;
Dr.-Phys. Krauze, Armands; Dr.-Phys. Virbulis, Jānis
Faculty of Physics and Mathematics
University of Latvia
Zellu str. 8, LV-1002 Riga, Latvia
E-mails: andrejs.sabanskis@lu.lv; kirils.surovovs@lu.lv; armands.krauze@lu.lv; janis.virbulis@lu.lv

Acknowledgements

This work is supported by European Regional Development Fund project Nr. 2013/0051/2DP/2.1.1.1.0/13/APIA/VIAA/009

MAGNETOHYDRODYNAMICS Vol. 51 (2015), No. 1, pp. 157–170

THREE-DIMENSIONAL MODELLING OF DOPANT TRANSPORT IN GAS AND MELT DURING FZ SILICON CRYSTAL GROWTH

A. Sabanskis, K. Surovovs, J. Virbulis

Faculty of Physics and Mathematics, University of Latvia,
8 Zellu str., LV-1002, Riga, Latvia

Three-dimensional (3D) steady-state modelling of inert gas flow and dopant transport in a floating zone puller has been carried out for the first time. The obtained results are analyzed regarding their effect on heat and dopant transfer and used to specify the concentration boundary conditions for 3D transient simulations of dopant transport in liquid silicon. The calculated radial resistivity variations in the crystal were compared with experiment.

Introduction. In the floating zone (FZ) growth of silicon (Si), single crystal [1, 2] doping from the atmosphere is commonly used. Numerical predictions of the electrical resistivity of the grown crystal are of particular importance because experiments are relatively expensive and provide only a limited information about the process. In the last decades, the increase of the available computing power allowed to perform an advanced and more precise modelling of the shape of Si phase boundaries, melt flow and dopant transport, see, e.g., [3–6].

The developed mathematical models are primarily validated by comparing the simulation results with the shapes of interfaces and radial resistivity variation (RRV) profiles in the grown crystal obtained in experiment. Generally, the predictions of numerical models qualitatively agree very well with experiment, whereas quantitative agreement is not perfect. This is also a case for the recent model developments presented in [7–9].

The existing mathematical models of the FZ process consider the main physical phenomena in an axisymmetric (heat transfer in Si, thermal radiation, shape of phase boundaries) or in a 3D (high-frequency electromagnetic field, melt flow) approach. Recently, the influence of axisymmetric gas flow on the shape of phase boundaries was investigated in [10] and on the dopant transport in the melt in [9]. However, the gas flow near the free melt surface cannot be precisely described by an axisymmetric model due to the 3D shape of the slitted inductor. Another important factor is the doping gas inlet, for which a 3D model is required.

In the present study, a 3D gas flow in a FZ puller was considered. The model describes a 3D steady-state gas and dopant (phosphine PH_3) flow driven by buoyancy and makes it possible to calculate the gas cooling effect at the Si boundaries as well as a dopant mass flux at the free melt surface and open melting front. The latter is used to specify the 3D boundary conditions for the calculations of the dopant transport in liquid Si. A successive calculation of the dopant transport in gas was performed using a more precise concentration boundary condition at the free surface from the liquid Si flow results. The computed RRV in the crystal is compared with experimental data.

1. Mathematical model and calculation algorithm.

1.1. Si phase boundaries. The program FZone, which is described in details in [5, 11], was used to calculate the axisymmetric quasi-stationary shape of Si phase boundaries. A 3D high-frequency electromagnetic field was also considered:

it was azimuthally averaged to obtain an induced power density distribution for the axisymmetric Si temperature calculations [12].

1.2. Gas flow. To describe the gas density ρ, the ideal gas law was used

$$\rho = p\frac{M_g}{RT}, \tag{1}$$

where p is the pressure, M_g is the molar mass of gas (39.948 g/mol for argon [13]), T is the absolute temperature, and $R = 8.314\,\mathrm{J/(mol{\cdot}K)}$ is the universal gas constant.

Note that the Boussinesq approximation cannot be used and a precise modelling of the gas density is needed because of the large temperature variations in the puller, which cause changes of ρ by a factor of 4. The velocity of the gas flow is by two orders of magnitude smaller than the speed of sound, therefore, a compressible flow in a low Mach number approximation is considered.

The Sutherland's law (2) is used to describe the dependence of the dynamic viscosity μ on the temperature. For argon, the values of the constants A_S and T_S are $2.130\,\mu\mathrm{Pa{\cdot}sK^{-1/2}}$ and 199.2 K, correspondingly [14].

$$\mu(T) = \frac{A_\mathrm{S}\sqrt{T}}{1 + T_\mathrm{S}/T}. \tag{2}$$

The steady-state gas flow is described by the continuity equation (3) and Navier–Stokes equations (4).

$$\mathrm{div}\,(\rho\mathbf{U}) = 0, \tag{3}$$

$$\mathrm{div}\,(\rho\mathbf{U}\otimes\mathbf{U} - 2\mu_\mathrm{eff}\,S_{ij}) + \mathrm{grad}\left(\frac{2}{3}\mu_\mathrm{eff}\,\mathrm{div}\mathbf{U}\right) = -\,\mathrm{grad}\,p_\mathrm{rgh} - \mathbf{gx}\,\mathrm{grad}\,\rho. \tag{4}$$

In these equations, $\mathbf{U}$ is the gas velocity, $\mathbf{g}$ is the gravity vector, $\mathbf{x}$ is the spatial position vector, $S_{ij} = (\partial U_i/\partial x_j + \partial U_j/\partial x_i)/2$ is the strain rate tensor. Turbulence is characterized by the effective viscosity $\mu_\mathrm{eff} = \mu + \mu_\mathrm{t}$, where μ is given by the Sutherland's law (2) and μ_t is calculated by a turbulence model. With the used OpenFOAM [15] implementation of the solver buoyantSimpleFoam, the pressure $p_\mathrm{rgh} = p - \rho\mathbf{gx}$.

The no-slip boundary condition for velocity is applied at the puller walls and at the inductor. The same boundary condition is also set at the Si surfaces – pulling and rotation of the crystals is neglected since the maximum linear velocities (roughly $6\cdot 10^{-5}$ m/s for pulling and 0.03 m/s for rotation) are much lower than a typical gas flow velocity of 1 m/s. It was taken into account for one case to evaluate the influence of the crystal rotation.

OpenFOAM implementation of the SST $k-omega$ turbulence model for compressible fluids with default model coefficients was used. The model equations for turbulent kinetic energy k and specific dissipation ω are the following [15, 16]:

$$\frac{\partial(\rho U_j k)}{\partial x_j} = \tilde{P} - \beta^*\rho\omega k + \frac{\partial}{\partial x_j}\left[(\mu + \sigma_k\mu_\mathrm{t})\frac{\partial k}{\partial x_j}\right],$$

$$\frac{\partial(\rho U_j\omega)}{\partial x_j} = \frac{\gamma\rho\tilde{P}}{\mu_\mathrm{t}} - \beta\rho\omega^2 + \frac{\partial}{\partial x_j}\left[(\mu + \sigma_\omega\mu_\mathrm{t})\frac{\partial\omega}{\partial x_j}\right] + 2(1 - F_1)\frac{\rho\sigma_{\omega 2}}{\omega}\frac{\partial k}{\partial x_j}\frac{\partial\omega}{\partial x_j},$$

where

$$\tilde{P} = \min\left(P, 10\beta^*\rho\omega k\right), \quad P = \tau_{ij}\frac{\partial U_i}{\partial x_j}, \quad \tau_{ij} = \mu_\mathrm{t}\left(2S_{ij} - \frac{2}{3}\frac{\partial U_k}{\partial x_k}\delta_{ij}\right) - \frac{2}{3}\rho k\delta_{ij},$$

$$\mu_\mathrm{t} = \frac{a_1\rho k}{\max(a_1\omega, SF_2)}, \quad F_1 = \tanh\left(\arg_1^4\right), \quad F_2 = \tanh\left(\arg_2^2\right),$$

$$\arg_1 = \min\left[\max\left(\frac{\sqrt{k}}{\beta^*\omega d}, \frac{500\mu}{d^2\rho\omega}\right), \frac{4\rho\sigma_{\omega 2}k}{\mathrm{CD}_{k\omega}d^2}\right], \quad \arg_2 = \max\left(2\frac{\sqrt{k}}{\beta^*\omega d}, \frac{500\mu}{d^2\rho\omega}\right),$$

$$\mathrm{CD}_{k\omega} = \max\left(2\rho\sigma_{\omega 2}\frac{1}{\omega}\frac{\partial k}{\partial x_j}\frac{\partial \omega}{\partial x_j}, 10^{-10}\right), \quad S = \sqrt{2S_{ij}S_{ij}},$$

d is the distance to the wall. The model constants are blended as $c = F_1 c_1 + (1 - F_1)c_2$, where $c = \gamma$, σ_k, σ_ω and β. The values of the constants are $\gamma_1 = 5/9$, $\gamma_2 = 0.44$, $\sigma_{k1} = 0.85$, $\sigma_{k2} = 1.0$, $\sigma_{\omega 1} = 0.5$, $\sigma_{\omega 2} = 0.856$, $\beta_1 = 0.075$, $\beta_2 = 0.0828$, $\beta^* = 0.09$, $a_1 = 0.31$.

The steady-state energy transfer is described by the enthalpy equation (5). In the equation, $\tilde{h} = c_p T$ is the specific enthalpy. The specific heat capacity at a constant pressure c_p is assumed constant. The effective thermal diffusivity for enthalpy $\alpha_\mathrm{eff} = \alpha + \alpha_\mathrm{t}$, where $\alpha_\mathrm{t} = \mu_\mathrm{t}/\mathrm{Pr}_\mathrm{t}$ is calculated by a turbulence model ($\mathrm{Pr}_\mathrm{t} = 1$), $\alpha = \mu/\mathrm{Pr}$ is the laminar thermal diffusivity for enthalpy, and Pr is the Prandtl number. For argon, $c_p = 520\,\mathrm{J/(kg{\cdot}K)}$ and $\mathrm{Pr} = 0.67$ [13].

$$\rho\mathbf{U}\,\mathrm{grad}\left(\tilde{h} + \frac{U^2}{2}\right) = \mathrm{div}\left(\alpha_\mathrm{eff}\,\mathrm{grad}\,h\right). \tag{5}$$

The first-type boundary conditions for temperature are applied at the puller walls, inductor and Si surfaces with reference to the FZone simulation results. The gas cooling heat flux density q is given by $q = -\alpha_\mathrm{eff}\,\partial\tilde{h}/\partial n$. The effect of argon cooling, however, has a negligible influence on the temperature distribution in the crystal and melt [10] and is neglected in the present study.

The steady-state dopant concentration field in gas C (dimensionless mass concentration) is described by the convection–diffusion equation

$$\rho\mathbf{U}\,\mathrm{grad}\,C = \mathrm{div}\left(\rho D_\mathrm{eff}\,\mathrm{grad}\,C\right), \quad \text{where} \quad \rho D_\mathrm{eff} = \frac{\mu}{\mathrm{Sc}} + \frac{\mu_\mathrm{t}}{\mathrm{Sc}_\mathrm{t}}, \tag{6}$$

where D is the diffusivity and Sc is the Schmidt number. As before, the index "eff" denotes the effective value and "t" the turbulent quantity. In the present study, constant Schmidt numbers were used: $\mathrm{Sc} = \mathrm{Sc}_\mathrm{t} = 0.7$. This choice was based on the following estimations: from theory, $\rho \sim T^{-1}$, $\mu \sim T^{0.5}$, $D \sim T^{1.5}$, therefore, $\rho D \sim T^{0.5} \sim \mu$. No values of D for the diffusion of phosphine in argon have been found in literature, but the data for other gases suggest that ρD is of the same order as μ.

The following boundary conditions for concentration were used: $C = 1$ at the doping gas inlet, $\partial C/\partial n = 0$ at the outlet, puller walls and inductor. $\partial C/\partial n = 0$ was also set at the solid silicon–gas boundary, since dopants can hardly penetrate from gas into solid silicon. At the molten Si-gas interfaces – free melt surface and open melting front – the concentrations in the melt and gas are related via complex relations. The concentration of phosphorus in the melt is proportional to the partial pressure of the doping gas (phosphine) and depends on the change of Gibbs energy and on the activity coefficient [17, 18]. Additionally, phosphorus can leave the melt by forming gaseous species P and P_2 and P_4 [18]. The flux of phosphorus atoms through the melt-gas interface is locally conserved. All these processes are described by simplified boundary conditions. First, it is assumed that $C = 0$ at the liquid silicon–gas boundary. Since this is a simplification, after

the dopant transport in liquid Si has been calculated, the boundary condition at the free melt surface for gas was replaced by a distribution proportional to the calculated C distribution in the melt. As the proportionality coefficient is not exactly known, simulations with $C_{\mathrm{gas}} = C_{\mathrm{melt}}$, $C_{\mathrm{gas}} = 6C_{\mathrm{melt}}$ and $C_{\mathrm{gas}} = 10C_{\mathrm{melt}}$ were performed. At the open melting front, zero concentration is assumed since the undoped Si is melted and penetrates the melt. To keep the notation short, the boundary conditions at the free melt surface in gas and in the melt are further denoted by C_{gas} and C_{melt}, respectively.

Using the calculated dopant concentration field, the dopant mass flux j at the melt free and open melting front surfaces was calculated as

$$j = -\rho D_{\mathrm{eff}} \frac{\partial C}{\partial n}. \tag{7}$$

1.3. Si melt flow. Transient 3D calculations of the melt flow were carried out using the solver FZSiFOAM, which has been developed previously and described in [19, 20]. The melt flow is considered as laminar, and the Boussinesq approximation is used to describe buoyancy. The non-stationary concentration field is described by the convection–diffusion equation

$$\frac{\partial C}{\partial t} + \mathbf{U}\,\mathrm{grad}\,C = D_0 \mathrm{div}\,\mathrm{grad}\,C, \tag{8}$$

where $D_0 = 3.29 \cdot 10^{-8}\,\mathrm{m}^2/\mathrm{s}$ is the diffusivity of the dopant concentration in liquid silicon. The ring-shaped profile for the dopant concentration and velocity at the melting interface (see Fig. 1) is used for $R_{\mathrm{ring}} \le r \le R_{\mathrm{ITP}}$ in a similar manner, as described in [8, 9, 20], however, in the present study, non-symmetric concentration boundary conditions are applied, as described below.

The non-symmetric ring-shaped profile at the melting interface: the concentration $C_{\mathrm{ring}}(\phi)$ for elements with azimuth $\phi_1 \le \phi \le \phi_2$ is found by integrating the dopant mass flux from gas flow calculations:

$$C_{\mathrm{ring}}(\phi) = \frac{1}{\rho_{\mathrm{l}} v_{\mathrm{ring}} S_{\mathrm{ring}}} \int_{R_{\mathrm{ITP}}}^{R_{\mathrm{f}}} \int_{\phi_1}^{\phi_2} j \,\mathrm{d}S, \tag{9}$$

where $v_{\mathrm{ring}} \gg v_{\mathrm{f}}$ is used to model the melt inflow through a thin fluid film (see Fig. 1), "f" denotes the feed rod, and ρ_{l} is the density of liquid Si. Integration is performed for circular sections of the open melting front. S_{ring} is the area of ring elements with the above mentioned azimuth:

$$S_{\mathrm{ring}} = \pi \left(R_{\mathrm{ITP}}^2 - R_{\mathrm{ring}}^2 \right) \frac{\phi_2 - \phi_1}{2\pi}. \tag{10}$$

A non-symmetric concentration flux at the melt free surface is applied according to the dopant mass flux from the gas flow calculations:

$$\frac{\partial C_{\mathrm{melt}}}{\partial n} = -\frac{j}{\rho_{\mathrm{l}} D_0}. \tag{11}$$

2. Results and discussion.

2.1. System description and calculation of phase boundaries. A FZ system with a crystal diameter of 51 mm from Leibniz Institute for Crystal Growth was considered [21]. The feed rod radius was 49 mm, the crystal pulling rate 3.4 mm/min, the inductor current frequency 3 MHz, the crystal and feed rod rotation rates were 6 rpm and 0.8 rpm, correspondingly. The length of the cylindrical part of the crystal and feed rod was set to 100 cm.

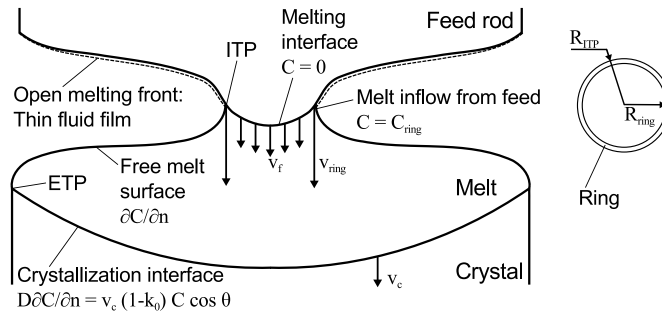

Fig. 1. Left: schematic of the FZ process and boundary conditions for concentration and velocity in 3D melt flow calculations; right: top view of the ring-shaped profile.

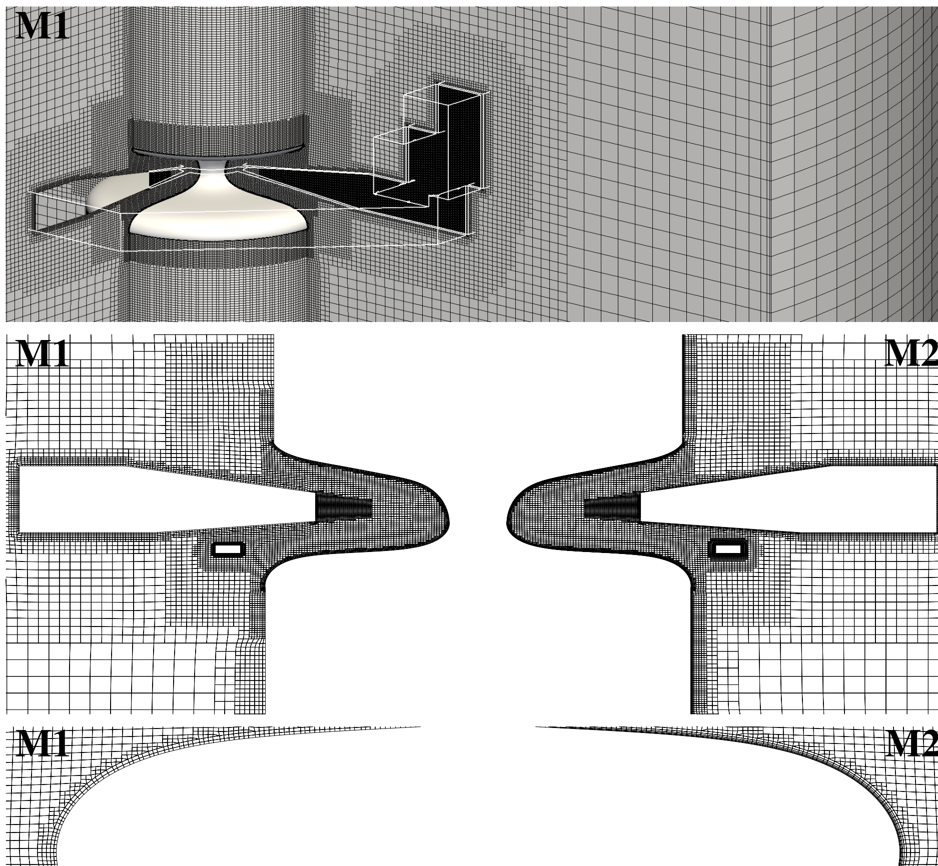

Fig. 2. Fragment of finite volume meshes M1 and M2 for gas flow calculations. Top: 3D view of the mesh M1 including inductor outline; middle: vicinity of the inductor; bottom – zoom at the boundary layers at the free melt surface.

The physical properties of silicon from [5] were used in the calculation of phase boundaries. A target zone height of 34.87 mm was ensured by adjusting the inductor current. The effect of melt flow was not taken into account.

2.2. Gas flow. The radius of the FZ puller was set to 30.0 cm and its height to 258.7 cm. An hex-dominant finite volume mesh M1, shown in Fig. 2, was created using the OpenFOAM mesh generator snappyHexMesh [15]. Three-dimensional Si and inductor surfaces were provided as an STL file. Additional mesh refinement

was applied in the vicinity of the Si and inductor surfaces. Boundary layers in the mesh were added to improve the near-wall resolution of flow boundary layers. The doping gas inlet was modeled as a cylinder with a diameter of 2 mm.

An additional mesh M2 (see Fig. 2) with refined boundary layers at the Si, inductor and puller wall surfaces and a refined mesh at the crystal were created to study the effect of the mesh size. The number of cells in the mesh M1 was about 7.9 million, and in M2 of 9.6 million. Several meshes with smaller number of elements were also tested, but they were found to be too rough. On the other hand, further mesh refinement was problematic due to low performance and memory limitations.

Calculations of the gas (argon) flow were carried out using the OpenFOAM standard solver buoyantSimpleFoam. The temperature of the inductor and puller walls was set to 400 K. A velocity of 0.26 m/s was applied at the inlet, which corresponds to a dopant volumetric flow rate of 50 cm^3/min.

Despite the fact that the steady state turbulence model was used, the calculated physical fields do not reach a steady state, but tend to fluctuate around their average values during iterations. This indicates that a part of the velocity fluctuations was not resolved by a turbulence model, however, transient modeling demanded too high computational resources for the used meshes and was not possible. Therefore, steady-state calculations were made, and to obtain time-averaged fields, the moving average was calculated over N=250 iterations. Additionally, to estimate the typical temperature fluctuations, the root-mean-square deviation was calculated for the temperature field as

$$\overline{T}_{\mathrm{RMSD}} = \sqrt{\frac{\sum (T_i - \overline{T})^2}{N}}, \tag{12}$$

where T_i is the temperature field at the i-th iteration, and $\overline{T}$ is the averaged temperature field. The summation is performed over N iterations.

An example of the computed averaged temperature field and its fluctuations in the vicinity of the inductor using the mesh M1 is shown in Figs. 3 and 4, correspondingly. The azimuthal angle ϕ defines the vertical cross-section of the domain: $\phi = 0°$ is the plane of the main inductor slit and it also contains the doping gas inlet (located at the opposite side of the main slit). The plane $\phi = 90°$ is perpendicular to the previous one and contains two (out of three) additional inductor slits. The planes at 45° and −45° contain the inductor cross-section, which was previously used in the axisymmetric gas flow calculations [9, 10].

The temperature field at $\phi = 0°$ and 90° shows that the upward gas flow through the additional slits of the inductor produces large temperature gradients at the open melting front and thus a noticeably stronger gas cooling in these

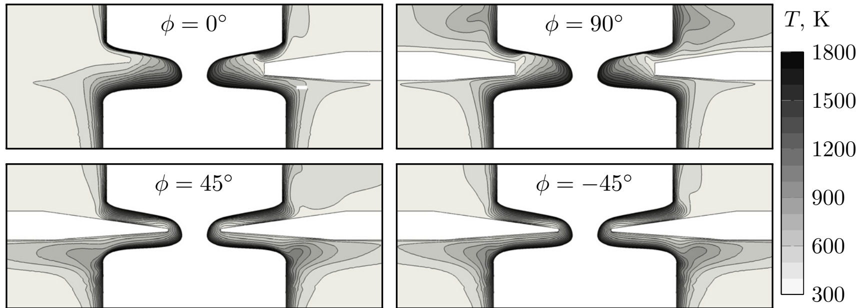

Fig. 3. The averaged temperature field in the vertical cross-sections. Mesh M1, spacing between isolines 100 K.

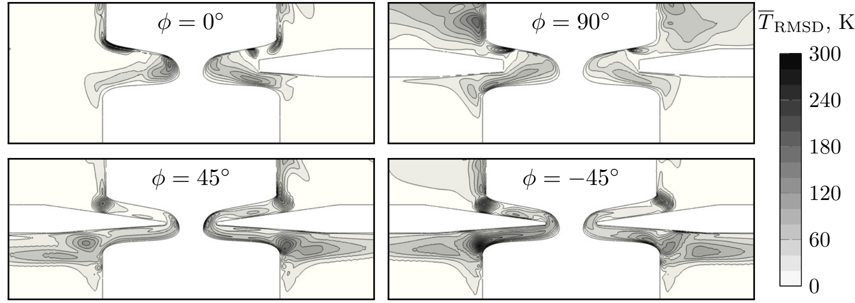

Fig. 4. Root-mean-square temperature deviation in the vertical cross-sections. Mesh M1, spacing between isolines 20 K.

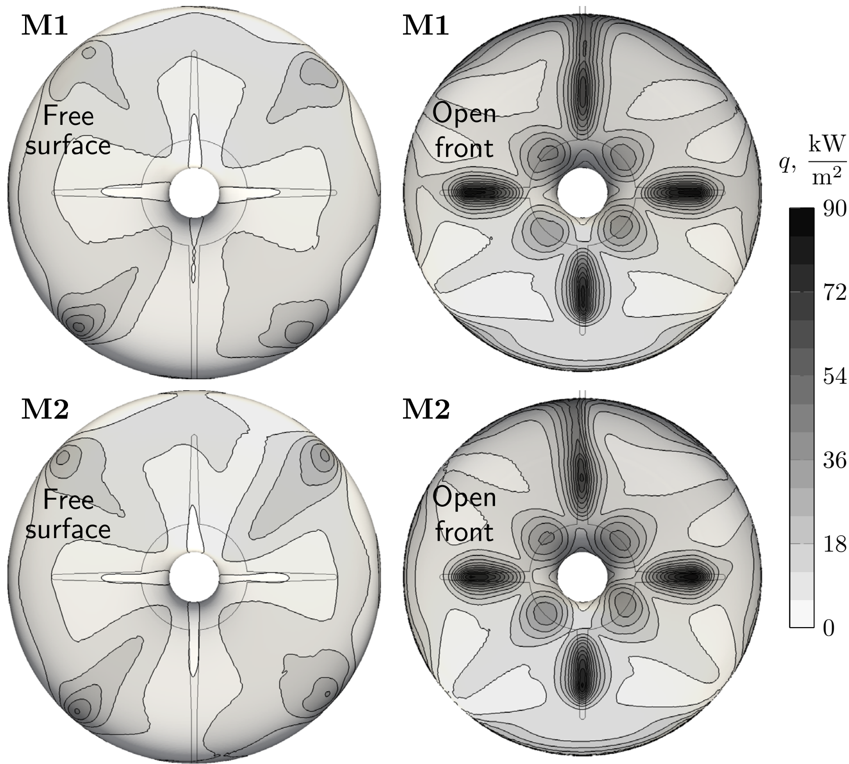

Fig. 5. Comparison of the heat flux density at the melt free surface (left) and at the open melting front (right) for meshes M1 (top) and M2 (bottom). Spacing between isolines 6 kW/m^2. Also shown is the position of the inductor slits.

regions. The results at $\phi = \pm 45°$ correspond well to the previous axisymmetric calculations. The slight asymmetry is caused by the doping gas inlet, which is located closer to the right part of the figures.

Despite of the relatively large characteristic values of $\overline{T}_{\mathrm{RMSD}}$ (50 ... 200 K), in the vicinity of solid walls, the temperature fluctuations decreased. It was observed that the typical fluctuations of instantaneous integral heat flux at the melt free surface and open melting front did not exceed 4% of their average value.

The boundary conditions and system geometry were symmetric with respect to the plane $\phi = 0°$. From physical considerations, it was expected for the averaged fields to have the same symmetry. It was verified (see Figs. 3, 4, 7 at $\phi = 90°$ and Figs. 5, 8) that the averaged fields were almost symmetric, whereas the in-

stantaneous fields were asymmetric (not shown). The observed deviations from symmetry for the averaged fields could be caused by a small number of averaging iterations.

The rotation of the crystal was taken into account for one case. For the crystal, the velocity boundary layer caused by its rotation was roughly 1.3 mm thick, and it was captured well by four layers of cells surrounding the crystal. However, a velocity magnitude of 0.03 m/s in the horizontal plane was significantly smaller than the vertical velocity component with a typical value of 1 m/s. Therefore, a noticeable influence of rotation was not found for the global velocity and temperature fields, as well as for the cooling heat flux densities at the Si surfaces.

To evaluate the mesh dependence, the results obtained on the meshes M1 and M2 were compared, paying attention to the resolution of the temperature and concentration boundary layers at the melt free surface and open melting front. The gas cooling heat flux density q at these surfaces is compared in Fig. 5. No significant mesh dependence was observed, which indicates that both meshes resolve well the temperature field. For the dopant mass flux j, which is shown in Fig. 8 in logarithmic scale, a minor mesh dependence was observed. However, in practical applications it is not crucial to precisely capture the changes of j over several orders of magnitude, therefore, it is concluded that the resolution of the C boundary layer by the mesh M1 is sufficient.

The structure of the heat flux density due to gas cooling shown in Fig. 5 is determined mainly by the inductor slits. The q maxima are located directly above the inductor slits and are caused by the strong vertical gas flow. The effect of gas cooling on the shape of the Si phase boundaries was neglected since it was weak: at the free melt surface, the average value of q was 13 kW/m^2 and the maximum value was 38 kW/m^2, while the characteristic value of the induced EM power density was 225 kW/m^2 and that of the net radiation heat flux density 100 kW/m^2. At the open melting front, these values were 19 kW/m^2, 89 kW/m^2, 750 kW/m^2 and 150 kW/m^2, respectively. The strong asymmetry at the latter surface might be important in 3D models of the FZ process, such as [22].

The previous axisymmetric gas flow calculations [10] were compared with 3D simulation results in Fig. 6. The planes $\phi = \pm 45°$ were examined for a 3D case, since they were located farthest away from the inductor slits and their cross-section corresponded to the axisymmetric geometry. The qualitative behavior of q was similar in both cases, however, 3D calculations predicted a significantly stronger gas cooling. It is believed that the quantitative differences are caused by

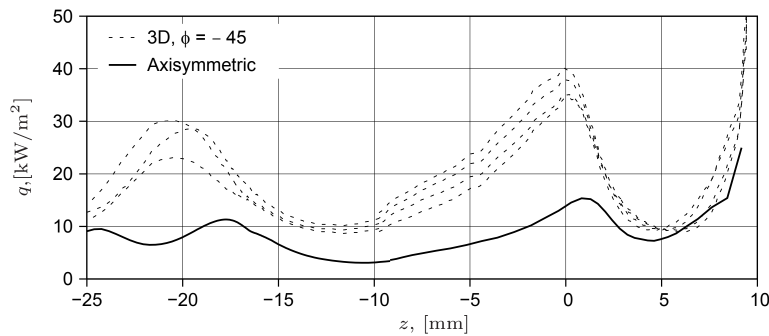

Fig. 6. Comparison of heat flux densities at the melt free surface ($z < -9$ mm) and at the open melting front ($z > -9$ mm) obtained in 3D calculations (mesh M1, $\phi = \pm 45°$) and using an axisymmetric approach [10].

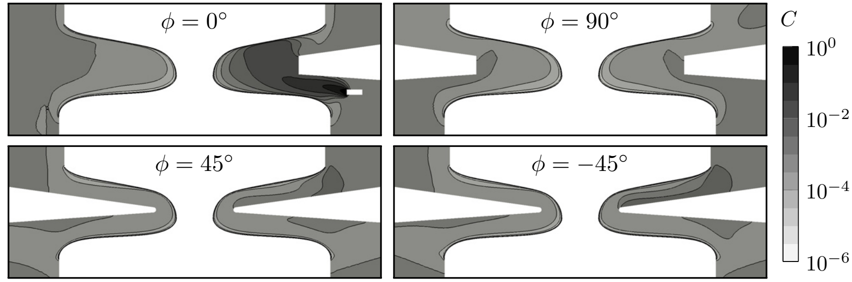

Fig. 7. The dopant concentration field in gas in the vertical cross-sections for C_{gas}=0. Mesh M1, logarithmic scale is used; two successive isovalues differ by a factor of 3.16.

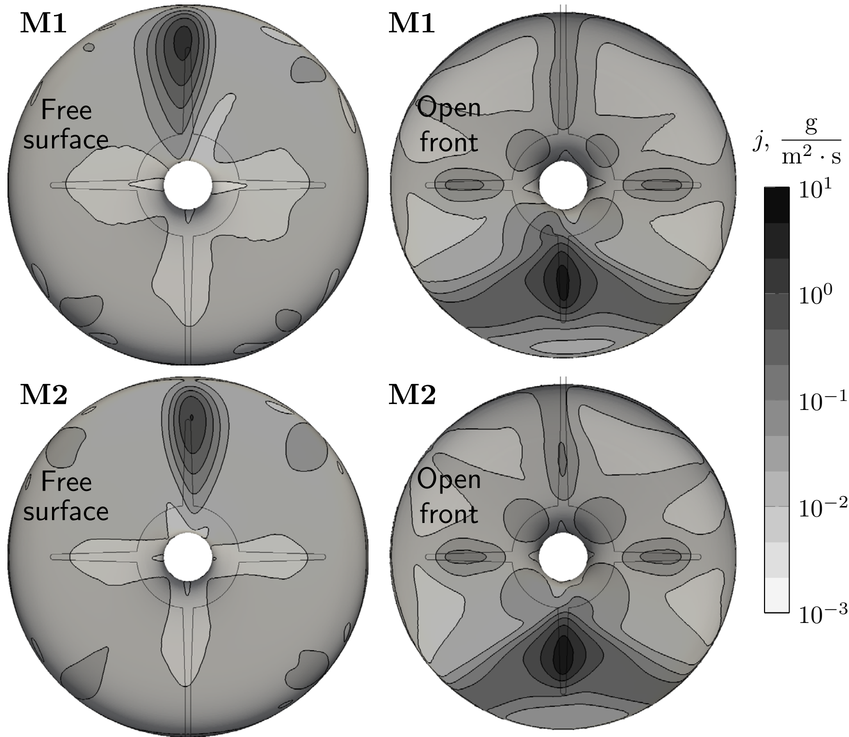

Fig. 8. Comparison of the dopant mass flux at the melt free surface (left) and at the open melting front (right) for meshes M1 (top) and M2 (bottom) for C_{gas}=0. Logarithmic scale is used; two successive isovalues differ by a factor of 2.15. Also shown is the position of the inductor slits.

the 3D shape of the inductor, which changes the flow pattern. The differences at $\phi = \pm 45°$, however, are not representative since, with slightly shifted angles, q decreases and is closer to the axisymmetric results.

The distribution of the dopant concentration field C in the vicinity of the inductor with $C_{\text{gas}} = 0$ is shown in Fig. 7. The logarithmic scale was used for a better view of the concentration boundary layers. The C distribution in the plane $\phi = 90°$ is almost symmetric. It can also be observed that with $\phi = \pm 45°$ the concentration above the inductor is higher in the right part of the figures, which indicates that this region is closer to the doping gas inlet.

Fig. 8 shows a dopant mass flux distribution at the melt free surface and open melting front for $C_{\text{gas}} = 0$. The distribution produced by the non-symmetric

doping gas inlet and inductor slits is strongly asymmetric. These results were used to specify the boundary conditions for 3D calculations of the dopant transport in a Si melt. These simulations, as well as additional dopant transport calculations in gas with updated boundary condition at the free melt surface are presented in subsection 2.3.

2.3. Melt flow. The Marangoni coefficient –0.13 mN/(m·K) and the segregation coefficient $k_0 = 0.35$ (phosphorus) were used in the simulations of the liquid Si flow and dopant transport. The ring-shaped profile was defined by $R_{\text{ring}} = 5.97$ mm, $R_{\text{ITP}} = 6.58$ mm, and by the velocity $v_{\text{ring}} = 0.02$ m/s.

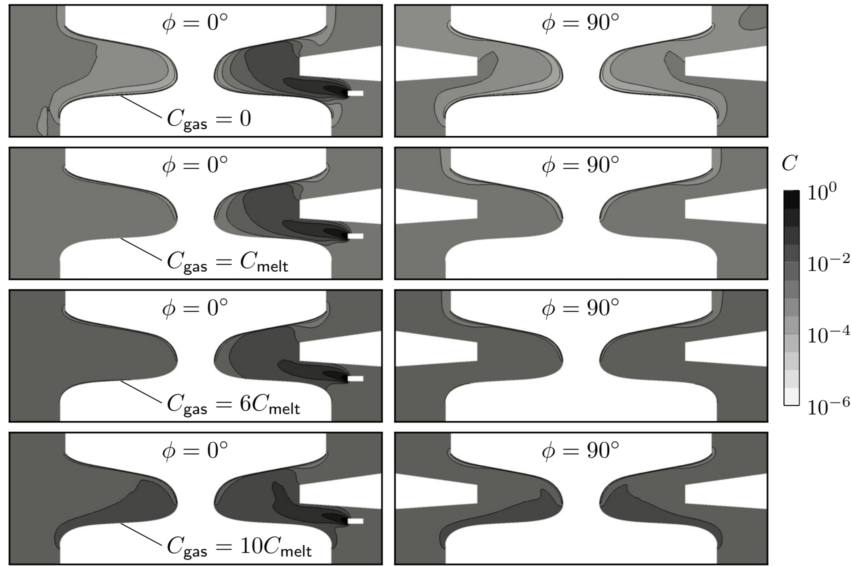

Fig. 9. The dopant concentration field in gas in the vertical cross-sections for different boundary conditions at the melt free surface. Mesh M1, logarithmic scale is used; two successive isovalues differ by a factor of 3.16.

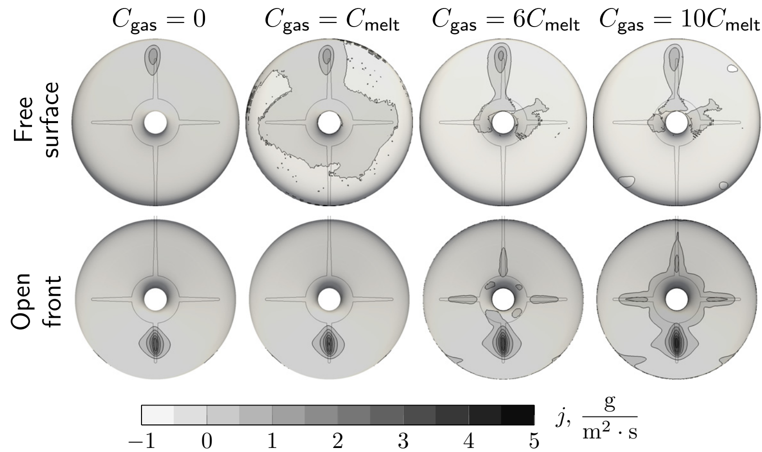

Fig. 10. Comparison of the dopant mass flux at the melt free surface (left) and at the open melting front (right). Mesh M1, different boundary conditions at the melt free surface. Spacing between isolines 0.5 g/m^{2}s. Also shown is the position of the inductor slits.

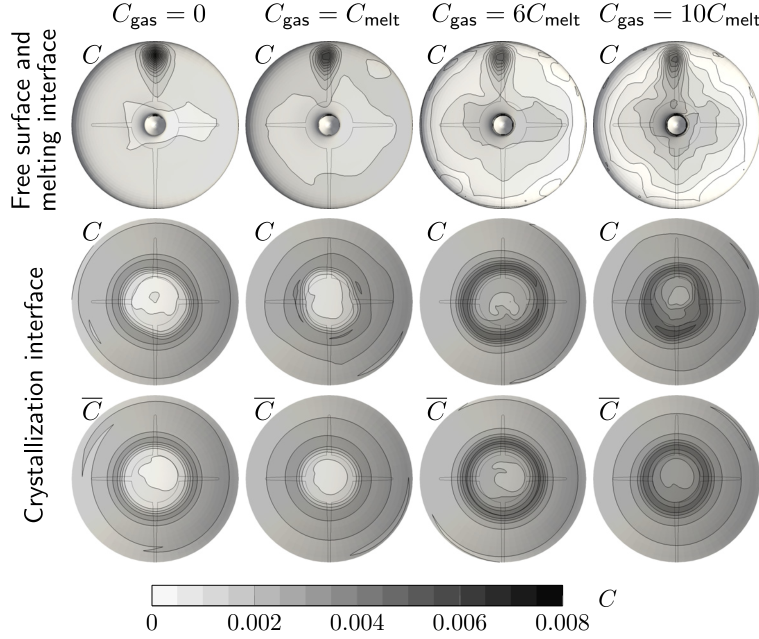

Fig. 11. Instantaneous and time-averaged concentration distributions at the melt free surface, melting and crystallization interfaces obtained by 3D HD calculations. Spacing between isolines $5 \cdot 10^{-4}$. Also shown is the position of the inductor slits.

The calculated concentration field for C_{gas}=0 is shown in the first column of Fig. 11. At the free melt surface, a pronounced C maximum can be seen caused by a direct flow of doping gas from the inlet. The structure of C isolines below the additional inductor slits resembles the same structure of j from the gas flow calculations. The non-symmetric concentration in the ring-shaped profile of the melting interface can also be observed. At the crystallization interface, on the other hand, the distribution of both instantaneous and averaged concentrations is azimuthally symmetric. This result evidences that despite of the non-symmetric boundary conditions, dopants are mixed well in the Si melt bulk. Therefore, the non-symmetric doping gas inlet still ensures that dopants incorporate symmetrically in a grown crystal.

At the melt free surface and open melting front, $C = 0$ was applied to the dopant transport in gas. This assumption is believed to hold well at the open melting interface, where an undoped Si feed rod is melted and flows towards the melt. In the molten zone and at the free surface, however, due to the phosphorus segregation at the crystallization interface, the increased concentration is typical and, therefore, back-coupling with C values from the dopant transport in liquid Si is needed. Since $C > 0$, a lower mass flux is expected at this surface. Additional concentration calculations in gas were made using the concentrations C_{melt}, $6C_{\mathrm{melt}}$ and $10C_{\mathrm{melt}}$ at the melt free surface. The last two conditions model a stronger reduction of j, even allowing dopants to get out of the melt, e.g., in the form of P and P_2 gas if the concentration in the melt is higher than in the gas. The obtained results are illustrated in Figs. 9 and 10.

With $C_{\mathrm{gas}} = 0$, the dopant mass flow rate from the gas to the free melt surface was $\dot{m}_{\mathrm{free}} = 0.47\,\mathrm{mg/s}$ and to the open melting front $\dot{m}_{\mathrm{of}} = 0.81\,\mathrm{mg/s}$. By setting $C_{\mathrm{gas}} = C_{\mathrm{melt}}$, the flow rates $\dot{m}_{\mathrm{free}}$ and $\dot{m}_{\mathrm{of}}$ were $0.20\,\mathrm{mg/s}$ and $1.07\,\mathrm{mg/s}$, respectively. With $C_{\mathrm{gas}} = 6C_{\mathrm{melt}}$, $\dot{m}_{\mathrm{free}}$ became negative, and the flow rates were

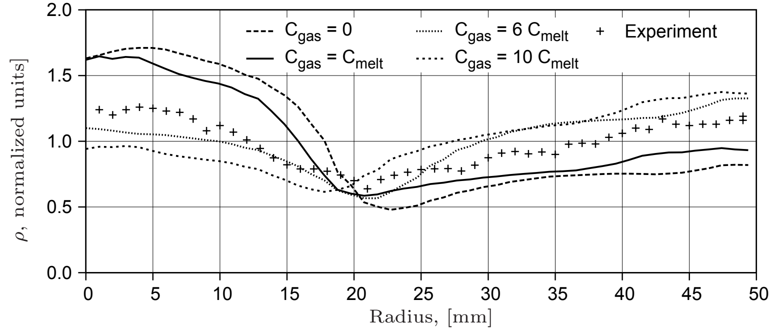

Fig. 12. Comparison of the calculated RRV profiles with experiment. Normalized units are used.

–1.09 mg/s and 2.38 mg/s, correspondingly. With $C_{\mathrm{gas}} = 10C_{\mathrm{melt}}$, the flow rates were $\dot{m}_{\mathrm{free}} = -2.13$ mg/s and $\dot{m}_{\mathrm{of}} = 3.42$ mg/s.

The calculated concentration field is shown in Fig. 11. At the melt free surface and at the melting interface the strong asymmetry is caused by the doping gas inlet and inductor slits (more pronounced for the latter two cases), however, a much more symmetric azimuthal distribution of both instantaneous and averaged concentrations was obtained at the crystallization interface. The considered cases with $C_{\mathrm{gas}} = 6C_{\mathrm{melt}}$ and $10C_{\mathrm{melt}}$ are not fully physical since the negative concentration values were observed at the outer parts of the melt. For all cases the calculated C_{melt} differs from C_{gas}, therefore, additional back-coupling iterations are needed for a consistent simulation of the dopant transport in gas and in the melt.

Fig. 12 depicts the calculated RRV profiles in the crystal. Comparison with experiment revealed that in the simulation with $C_{\mathrm{gas}} = 0$ the resistivity was overestimated for radial positions below 20 mm and underestimated for larger radii. The case with $C_{\mathrm{gas}} = C_{\mathrm{melt}}$ was closer to experiment, but still the agreement is unsatisfactory. By setting $C_{\mathrm{gas}} = 6C_{\mathrm{melt}}$ and $10C_{\mathrm{melt}}$, the resistivity “inverted” with respect to experiment: ρ was underestimated for $r < 20$ mm and overestimated for larger radii. An additional back-coupling iteration for $C_{\mathrm{gas}} = 6C_{\mathrm{melt}}$, taking the concentration for gas flow calculations from the obtained melt flow results, was carried out, followed by a melt flow calculation. The differences of $\dot{m}_{\mathrm{free}}$ and $\dot{m}_{\mathrm{of}}$ from the previously calculated values were only 9% and 5%, respectively, and no noticeable changes were observed for the RRV profiles. This evidences that one back-coupling iteration is sufficient. It is expected that calculations with $C_{\mathrm{gas}} \approx (3\ldots4)\,C_{\mathrm{melt}}$ would yield a good agreement with experiment.

3. Conclusions. In the current study, 3D gas flow calculations during a FZ growth of Si crystals have been carried out for the first time. The mesh generator snappyHexMesh from the open source library OpenFOAM is well-suited for 3D mesh generation in a complex geometry of the FZ puller with the axially symmetric puller wall and distinct refinement near the molten zone.

The calculated flow, temperature and concentration fields are strongly three-dimensional due to the 3D shape of the slitted inductor. A fairly good symmetry with respect to the plane of the main inductor slit is obtained for averaged fields, as expected. 3D calculations predict a stronger gas cooling than in previous axisymmetric simulations, the differences are caused by the change of the gas flow pattern by the inductor slits.

3D dopant transport simulations show distinct concentration maxima on the melt free surface and at the open melting front at the side of the dopant inlet. Despite of this non-symmetry, the dopant distribution at the crystallization interface is rather symmetric. The best agreement with experiment could be obtained in the case of $C_{\mathrm{gas}} \approx (3 \ldots 4)\, C_{\mathrm{melt}}$, which means that a more precise modelling of surface chemistry is necessary in future simulations.

Acknowledgements. The present work was supported by the European Regional Development Fund, project contract No. 2013/0051/2DP/2.1.1.1.0/13/-APIA/VIAA/009.

REFERENCES

[1] W. Zulehner. Historical overview of silicon crystal pulling development. *Materials Science and Engineering B: Solid-State Materials for Advanced Technology*, vol. 73 (2000), no. 1, pp. 7–15.

[2] T. Duffar, editor. *Crystal Growth Processes Based on Capillarity* (John Wiley,& Sons, Ltd, 2010).

[3] A. Mühlbauer, *et al.* Interface shape, heat transfer and fluid flow in the floating zone growth of large silicon crystals with the needle-eye technique. *Journal of Crystal Growth*, vol. 151 (1995), no. 12, pp. 66 –79.

[4] T.L. Larsen. Phosphorus diffusion in float zone silicon crystal growth. Ph.D. thesis, Technical University of Denmark, 2000.

[5] G. Ratnieks. Modelling of the floating zone growth of silicon single crystals with diameter up to 8 inch. Ph.D. thesis, Rīga: University of Latvia, 2007.

[6] K. Lācis. 3D modeling of influence of magnetic fields in floating zone crystal growth. Ph.D. thesis, Rīga: University of Latvia, 2010.

[7] A. Sabanskis, *et al.* Modelling of the influence of electromagnetic force on melt convection and dopant distribution during floating zone growth of silicon. *Proceedings of the 9th International Conference on Fundamental and applied MHD, Thermo acoustic and Space technologies*, (2014), pp. 186 –190.

[8] K. Surovovs, A. Muiznieks, A. Sabanskis, and J. Virbulis. Hydrodynamical aspects of the floating zone silicon crystal growth process. *Journal of Crystal Growth*, vol. 401 (2014), pp. 120–123. Proceedings of 17th International Conference on Crystal Growth and Epitaxy (ICCGE-17).

[9] A. Sabanskis, K. Surovovs, A. Krauze, and J. Virbulis. Modelling of dopant transport during floating zone growth of silicon. *Proceedings of the International Scientific Colloquium "Modelling for Electromagnetic Processing"*, (2014), pp. 99–104.

[10] A. Sabanskis and J. Virbulis. Simulation of the influence of gas flow on melt convection and phase boundaries in FZ silicon single crystal growth. *Journal of Crystal Growth*, (2014). http://dx.doi.org/10.1016/j.jcrysgro.2014.07.041.

[11] G. Ratnieks, A. Muižnieks, and A. Mühlbauer. Modelling of phase boundaries for large industrial FZ silicon crystal growth with the needle-eye technique. *Journal of Crystal Growth*, vol. 255 (2003), no. 34, pp. 227–240.

[12] A. Muiznieks, A. Rudevics, H. Riemann, and U. Lacis. Comparison between 2D and 3D modelling of HF electromagnetic field in FZ silicon crystal growth process. *Proceedings of the International Scientific Colloquium "Modelling for Material Processing"*, (2010), pp. 61–65.

[13] D.R. Lide, editor. *CRC Handbook of Chemistry and Physics* (CRC Press, 2003).

[14] E. Bich, J. Millat, and E. Vogel. The viscosity and thermal conductivity of pure monatomic gases from their normal boiling point up to 5000 K in the limit of zero density and at 0.101325 MPa. *Journal of physical and chemical reference data*, vol. 19 (1990), no. 6, pp. 1289–1305.

[15] The open source CFD toolbox OpenFOAM. `http://www.openfoam.org/`, February 5th, 2015.

[16] Langley research center turbulence modeling resource. `http://turbmodels.larc.nasa.gov/sst.html`, February 5th, 2015.

[17] A. Vorobev, A. Sidko, and V. Kalaev. Advanced chemical model for analysis of Cz and DS Si-crystal growth. *Journal of Crystal Growth*, vol. 386 (2014), pp. 226–234.

[18] S. Zheng, T. Engh, M. Tangstad, and X.-T. Luo. Numerical simulation of phosphorus removal from silicon by induction vacuum refining. *Metallurgical and Materials Transactions A*, vol. 42 (2011), no. 8, pp. 2214–2225.

[19] A. Rudevics, *et al.* Using of open source code library OpenFOAM for 3D magnetohydrodynamic calculations in semiconductor crystal growth technologies. *Proceedings of the International Scientific Colloquium "Modelling for Material Processing"*, (2008), pp. 103–108.

[20] K. Lācis, A. Muižnieks, A. Rudevičs, and A. Sabanskis. Influence of DC and AC magnetic fields on melt motion in FZ large Si crystal growth. *Magnetohydrodynamics*, vol. 46 (2010), no. 2, pp. 199–218.

[21] H.-J. Rost, R. Menzel, A. Luedge, and H. Riemann. Float-zone silicon crystal growth at reduced RF frequencies. *Journal of Crystal Growth*, vol. 360 (2012), pp. 43–46. 5th International Workshop on Crystal Growth Technology.

[22] M. Plāte, A. Krauze, and J. Virbulis. 3D simulation of feed rod melting in floating zone silicon single crystal growth. *Magnetohydrodynamics*, vol. 51 (2015), no. 1.

Received 17.02.2015

Journal of Crystal Growth 401 (2014) 120–123

Contents lists available at ScienceDirect

Journal of Crystal Growth

journal homepage: www.elsevier.com/locate/jcrysgro

Hydrodynamical aspects of the floating zone silicon crystal growth process

Kirils Surovovs [a,b,*], Andris Muiznieks [b], Andrejs Sabanskis [b], Janis Virbulis [b]

[a] Institute of Solid State Physics, University of Latvia, Kengaraga str., Riga, LV-1063, Latvia
[b] Faculty of Physics and Mathematics, University of Latvia, Zellu str. 8, Riga, LV-1010, Latvia

A R T I C L E I N F O

Available online 28 January 2014

Keywords:
A1. Computer simulation
A1. Hydrodynamics
A2. Floating zone technique
A2. Single crystal growth
B2. Semiconducting silicon

A B S T R A C T

3D numerical modeling of dopant transport in the melt is carried out for the 100 mm floating zone silicon single crystal growth process. The axis-symmetric shape of the molten zone is calculated with the program *FZone* considering the coil and the high frequency (HF) electromagnetic (EM) field in 3D. Time dependent melt flow, temperature and dopant concentration fields are modeled using a specialized solver based on the open source code library OpenFOAM®. The influence of the Marangoni coefficient in the boundary conditions on the melt velocity field is analyzed. The obtained shapes of the crystallization interface and resistivity profiles in the grown crystal are compared with experimental results. Differences between axis-symmetric and non-symmetric models are analyzed.

© 2014 Elsevier B.V. All rights reserved.

1. Introduction

There are two main methods of growing silicon (Si) single crystals for microelectronics – the Czochralski (CZ) method and the Floating zone (FZ) method. The experiments of Si single crystal growth process carried out for the process development are very expensive therefore numerical modeling is frequently used to support the process improvement. Computational resources allow to model many physical aspects of a FZ system, e.g., hydrodynamical (HD) processes in liquid silicon, that cannot be revealed by performing experiments.

In this study the calculations of phase boundaries are performed with the previously developed program *FZone* [1], where all interfaces and fields are calculated in axially symmetrical approximation (2D), except the 3D HF EM field of non-symmetrical inductor. The influence of the melt flow on 2D shape of phase boundaries can be investigated using *FZone* as well. The other program used — 3D solver *FZSiFOAM* for the melt flow, temperature and dopant concentration distribution based on the open source code library OpenFOAM® is described in [2]. However, the results of this program were not verified by experiments, e.g., compared with measured radial resistivity variations (RRV).

Although many numerical models are successfully used to describe the FZ crystal growth process it is necessary to improve them using new available experimental data. In the present work HD modeling is used to obtain a more precise shape of phase boundaries and for the calculation of RRV profiles from the dopant concentration field in the melt. This allows to investigate the influence of the temperature coefficient of surface tension $M = \partial\gamma/\partial T$ (i.e., Marangoni coefficient), which has strong dependence on the oxygen content in growth chamber [3].

2. Description of experimental FZ system

The experiments have been carried out in the Leibniz Institute for Crystal Growth by Robert Menzel who investigated the influence of a lower frequency of the induction coil on the FZ process [4]. The parameters of the experimental system are listed in Table 1 and the inductor used is shown in Fig. 1.

Table 1
Parameters of the experimental system.

Parameter, unit of measurement	Value
Radius of crystal R_C, mm	51
Radius of feed rod R_F, mm	49
Zone height H_Z, mm	34.87
Pull rate of crystal v_C, mm/min	3.4
Pushing rate of feed rod v_F, mm/min	3.68
Frequency of current in inductor f_{ind}, MHz	3
Rotation speed of crystal ω_C, rpm	6
Rotation speed of feed rod ω_F, rpm	0.8

* Corresponding author at: Faculty of Physics and Mathematics, University of Latvia, Zellu str. 8, Riga LV-1002, Latvia. Tel.: +371 29 84 02 54.
E-mail address: ks10172@lu.lv (K. Surovovs).

0022-0248/$ - see front matter © 2014 Elsevier B.V. All rights reserved.
http://dx.doi.org/10.1016/j.jcrysgro.2013.12.066

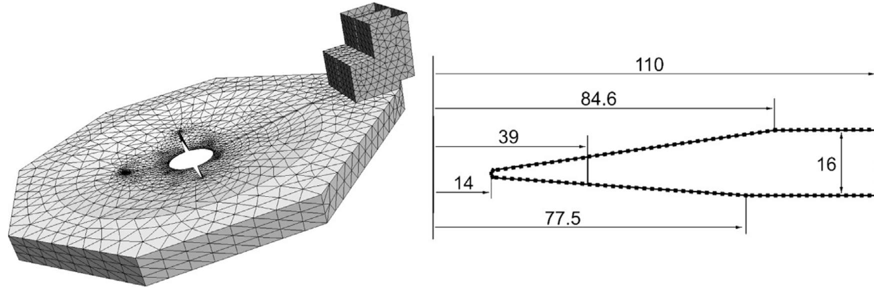

Fig. 1. Overall view of the HF inductor (left) and its geometrical dimensions of the vertical cross-section (right).

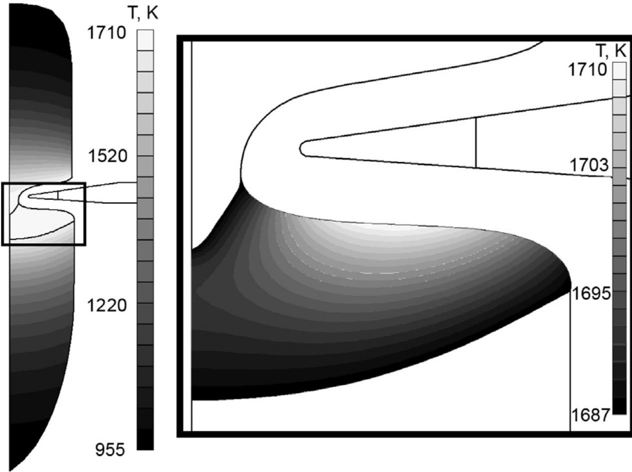

Fig. 2. Calculated phase boundaries and obtained temperature field using the program *FZone* [1].

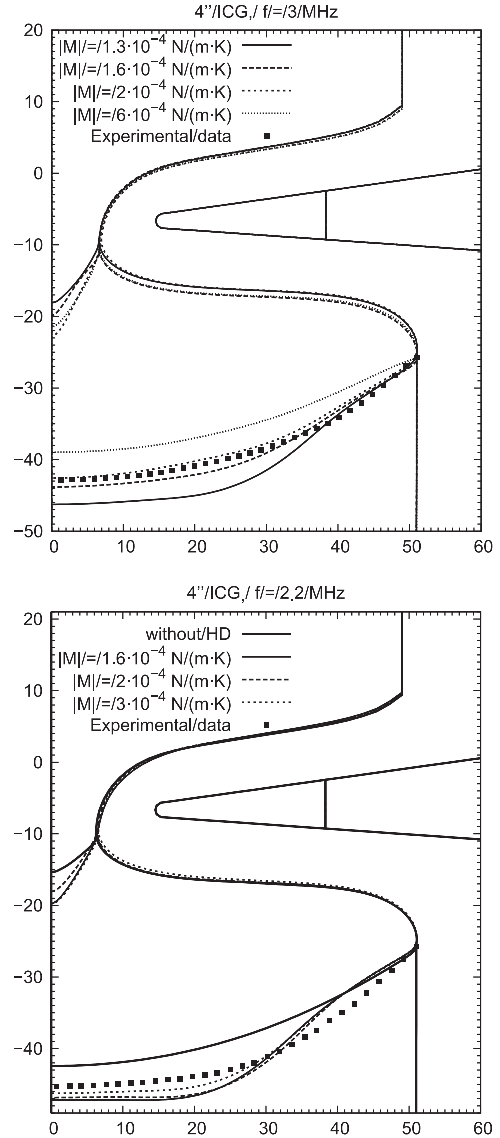

Fig. 3. Phase boundaries in the 4 inch FZ system for $f_{ind} = 3$ MHz (top) and $f_{ind} =$ 2.2 MHz (bottom).

3. Mathematical models and software

3.1. Phase boundaries

The first step of the numerical modeling of the FZ crystal growth process is 2D axis-symmetric calculations of phase boundaries using a specialized program *FZone* [1]. The calculations of the HF EM field are done considering the 3D HF inductor [5]. The obtained induced power surface density values are averaged in the azimuthal direction so that they can be used as a heat source for the 2D axis-symmetric phase boundary calculations. Melt motion (incompressible, laminar, buoyancy-driven flow) can be taken into account. The position of the phase boundaries is found iteratively starting from some initial approximation. The direction and magnitude of the movement of any interface point depends on the equations of heat balance where temperature gradients are obtained from the calculated temperature field [1]. An axially symmetrical approximation of melt flow is used due to the large number of iterations required — for every shape of phase boundaries the temperature field must be solved (Fig. 2).

3.2. Melt flow

The unsteady 3D numerical modeling of the melt flow in the FZ process is performed with the solver *FZSiFOAM* which is based on the open source code library OpenFOAM. For the calculations a structured mesh of 160,000 hexahedral elements was used. The melt flow is considered as laminar as the characteristic Reynolds number is approximately 1500. The detailed description of the used mathematical models is given in [6], only the most important equations are listed here:

$$\rho_0\frac{\partial \mathbf{v}}{\partial t}+\rho_0(\mathbf{v}\nabla)\mathbf{v} = -\nabla p+\eta\Delta\mathbf{v}-\rho_0\mathbf{g}\beta(T-T_0),$$

$$\nabla\mathbf{v}=0,$$

$$\rho_0 c_p\frac{\partial T}{\partial t}+\rho_0 c_p(\mathbf{v}\nabla)T=\lambda\Delta T,$$

where ρ_0 is the density of liquid silicon at melting temperature, $\mathbf{v}$ — melt velocity, t — time, p — pressure, η — dynamic viscosity, $\mathbf{g}$ —

acceleration of gravity, β — thermal volume expansion coefficient, T — temperature, T_0 — melting temperature of silicon, c_p — specific heat and λ — thermal conductivity. The buoyancy forces are described using the Boussinesq approximation. The crystallization interface is considered as outlet with the following boundary conditions for the velocity: $v_z = -v_C$, $v_r = 0$, $v_\phi = 2\pi r \omega_C$ (in cylindrical coordinates, $x = r\cos\phi$ and $y = r\sin\phi$). The melting interface is considered as inlet and the desired mass inflow is set equal to the outflow through the crystallization interface. A ring-shaped profile is used for v_z to simulate melt flow from the open melting front through the thin melt film (see Fig. 5). The Marangoni force distribution recalculated in every time step using the temperature distribution and EM force distribution received from the 3D HF EM calculations is used for boundary conditions for the melt velocity on the free melt surface:

$$f = \frac{1}{4}\mu_0 \delta \nabla_s j^2 + M \nabla_s T,$$

where f is the boundary stress, $\delta = \sqrt{\pi f_{\text{ind}} \sigma \mu_0}$ is the thickness of a skin layer, ∇_s is surface gradient, j is the surface current density and σ is the conductivity of liquid silicon conductivity.

For the dopant concentration field (C) the following mass transport equation is solved:

$$\frac{\partial C}{\partial t} + (\mathbf{v}(t)\nabla)C = D\Delta C, \quad (1)$$

where D is the diffusion coefficient of dopants. From the calculated C distribution at the crystallization interface the RRV can be obtained: $\rho = 1/k_0 C$, where ρ is the resistivity and k_0 is the segregation coefficient. Boundary conditions for the concentration are:

(a) on the crystallization interface $D\partial C/\partial n = v_C(1-k_0)C\cos\theta$, where n is the normal coordinate, k_0 is the segregation coefficient and θ is the angle between the XY (horizontal) plane and the interface normal vector;
(b) on the melt free surface due to the assumption of homogeneous concentration distribution in argon atmosphere a constant concentration is normalized to $C = 1$;
(c) on the melting interface — ring-shaped profile, where dopant concentration at ring is equal to concentration on free surface, and silicon feed rod is considered pure ($C = 0$) (see Fig. 5).

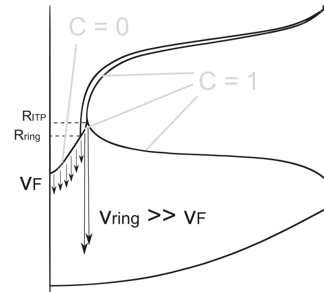

Fig. 5. Schematic representation of boundary conditions for the melt velocity and dopant concentration.

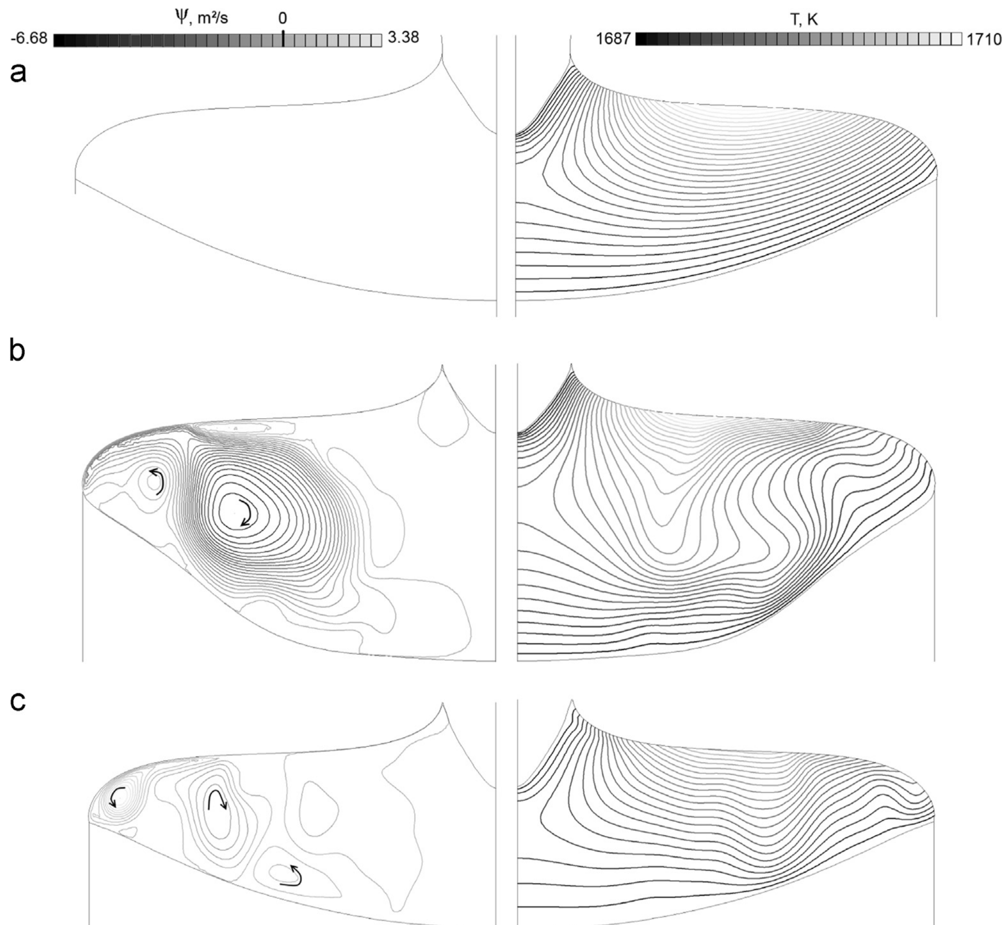

Fig. 4. Axially symmetrical results of the *FZone* program. Stream function (on the left) and temperature (right), for cases without melt flow calculations (a), with $|M| = 1.3 \times 10^{-4}$ N/m K (b) and with $|M| = 6 \times 10^{-4}$ N/m K (c).

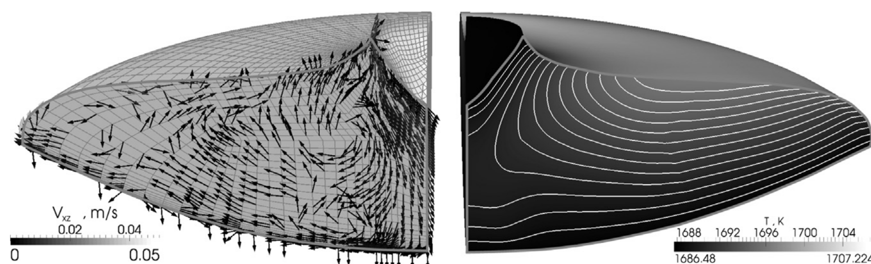

Fig. 6. Hexahedral mesh with velocity vectors (left) and temperature distribution (right) obtained with *FZSiFOAM*, $|M| = 1.3 \times 10^{-4}$ N/m K.

4. Results and conclusions

The phase boundaries obtained with the *FZone* program for a 3 MHz EM field are shown in Fig. 3, on the top. Calculations with different Marangoni coefficients were carried out as the exact value of it is not precisely known. This is mainly due to the strong dependence of the Marangoni coefficient on oxygen content even at small oxygen concentrations which are hard to measure. To explain the differences in the calculated deflections of crystallization interface the biggest central vortex has to be looked at (Fig. 4b). EM forces are "pulling" the melt along the free surface from the crystal and feed rod to the central part of the surface where it is located closer to the inductor. Marangoni forces $F_M = M\nabla T$ are "pulling" the melt in the opposite direction from hot to cold regions because M is negative. If $|M|$ is small, EM forces dominate and create a big vortex which makes Si flow from the temperature maximum at the free surface downwards towards the crystallization interface. The temperature field is strongly distorted in comparison to the calculation that does not account for the HD processes in the melt (see Fig. 4a). The vortex transports the heat towards the crystallization interface and therefore the position of the interface is moved further from the free surface. When $|M|$ increases the influence of the EM forces decreases as they become partly compensated by Marangoni forces and the main vortex becomes weaker (Fig. 4c). From these results it can be concluded that the most realistic M number is about -2×10^{-4} N/m K. According to [3], it corresponds to O_2 partial pressure $p(O_2) \approx 10^{-11}$ Pa. However, this result cannot be verified, as the oxygen content in atmosphere was not measured during the experiment [4].

Fig. 3, on the bottom, shows the results for the reduced frequency of 2.2 MHz. Two experimentally observed tendencies – deepening and bending of the crystallization interface – are present in the results of the calculations. Although none of the calculated boundaries show good agreement with the experimentally obtained shape, the calculated shapes have more pronounced bending. The reason for larger disagreement could be the changed volumetric distribution of EM heat sources and EM forces (increased skin layer thickness), which are assumed only on the surface in the *FZone* program.

Based on axially symmetric phase boundaries, calculated in *FZone* without the melt flow, the 3D hydrodynamical calculations via *FZSiFOAM* were carried out to get RRV profiles in the crystal. The calculated melt velocity and temperature fields as well as the used hexahedral mesh for the case of $|M| = 1.3 \times 10^{-4}$ N/m K are shown in Fig. 6.

The distributions of RRV at the crystallization interface for different M are shown in Fig. 7. The best correspondence to experimental RRV is achieved using $|M| = 1.3 \times 10^{-4}$ N/m K ($p(O_2) \approx 10^{-9}$ Pa, according to [3]). This M value is smaller than the value of the best agreement for crystallization interface deflection. The difference could be explained by the usage of an axis-symmetric (*FZone*) model for the calculation of the interface shape and 3D (*FZSiFOAM*) model for the RRV distribution.

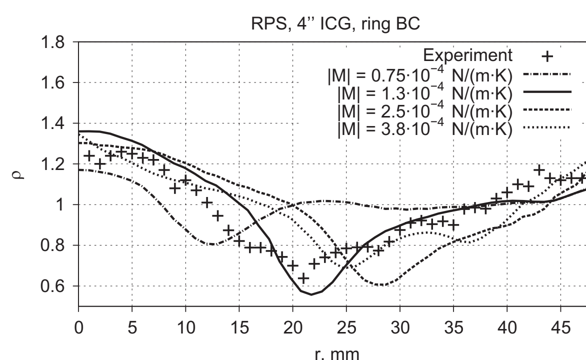

Fig. 7. Radial resistivity variation profiles in grown crystal.

Acknowledgments

The present work is carried out at the University of Latvia and has been supported by the European Regional Development Fund project: No. 2010/0245/2DP/2.1.1.1.0/10/APIA/VIAA/114.

Funding sources had no involvement in preparing, writing and submitting the present paper.

References

[1] G. Ratnieks, A. Muiznieks, A. Muhlbauer, Modelling of phase boundaries for large industrial FZ silicon crystal growth with the needle-eye technique, J. Cryst. Growth 255 (2003) 227–240.

[2] A. Rudevics, K. Lacis, A. Muiznieks, N. Jekabsons, B. Nacke, Using of open source code library OpenFOAM for 3D magnetohydrodynamic calculations in semiconductor crystal growth technologies, Modell. Electromagnet. Process. (2008) 103–108.

[3] Z.F. Yuan, K. Mukai, W.L. Huang, Surface tension and its temperature coefficient of molten silicon at different oxygen potentials, Langmuir 18 (6) (2002) 2054–2062.

[4] H.-J. Rost, R. Menzel, A. Luedge, H. Riemann, FZ silicon crystal growth at reduced RF frequencies, J. Cryst. Growth 360 (2012) 43–46.

[5] A. Muižnieks, A. Rudevičs, H. Riemann, U. Lācis. Comparison between 2D and 3D modelling of HF electromagnetic field in FZ silicon crystal growth process. International Scientific Colloquium Modelling for Material Processing, Rīga, 2010, pp. 61–65.

[6] A. Muiznieks, K. Lacis, B. Nacke, 3D unsteady modeling of the melt flow in the FZ silicon crystal growth process, Magnetohydrodynamics 43 (2007) 3–12.

MODELLING OF THE INFLUENCE OF ELECTROMAGNETIC FORCE ON MELT CONVECTION AND DOPANT DISTRIBUTION DURING FLOATING ZONE GROWTH OF SILICON

SABANSKIS[1] Andrejs, SUROVOVS[1,2] Kirils, KRAUZE[1] Armands, PLATE[1] Matiss, VIRBULIS[1] Janis
Affiliation: [1]Faculty of Physics and Mathematics, University of Latvia, Zeļļu str. 8, LV-1002, Riga, Latvia
[2]Institute of Solid State Physics, University of Latvia, Ķengaraga str. 8, LV-1063, Riga, Latvia
E-mail address of corresponding author: kirils.surovovs@lu.lv

Abstract: Numerical modelling of floating zone process is considered. A local analysis of the electromagnetic (EM) field distribution in the vicinity of the external triple point (ETP) was carried out using the complex vector potential formulation and the result was included in the calculation of phase boundaries, to improve the surface current formulation. 3D hydrodynamic (HD) calculations were performed using the open source code library *OpenFOAM*. The influence of high-frequency EM field is shown by comparing phase boundaries, convection in melt and radial resistivity variation profiles. The results are compared with experimental data.

1. Introduction

There are two main methods of growing silicon single crystals for microelectronics – the Czochralski (CZ) method and the floating zone (FZ) method. Crystals grown with CZ method have relatively high dopant concentration, due to contact between silicon melt and quartz crucible. On the other hand, the FZ process is appropriate for power electronics (high purity crystals), because molten silicon is not in contact with other materials.

In FZ method high-frequency (HF) inductor is used to melt polycrystalline silicon feed rod. It induces currents in silicon (see Fig. 1, left), that flows only in a thin skin layer due to high frequency of alternating inductor current, typically about 3 MHz. Being pulled by gravity, molten silicon flows downwards through the hole at the middle of inductor and forms a large droplet due to a relatively high surface tension.

At some distance below the inductor, where induced EM power is lower, molten silicon crystallizes due to radiative heat losses. It forms a single crystal, because the characteristic velocities of this process are very low – several millimetres per minute. FZ method is realized in the atmosphere of noble gases (usually argon). Before the 8th decade of XX century only small diameter crystals were grown, but “needle-eye” technique, in which radii of crystal and feed rod are much greater than inner radius of induction coil (see Fig. 1, right), allowed to reach even 200 mm diameter. This is more convenient for industrial purposes, because many elements can be created and etched on a single wafer (i.e. on a thin silicon disc), but growth process becomes more complicated for bigger crystal diameter.

To develop the FZ process, numerical modelling can be used. Its advantages are inexpensiveness and possibility to reveal some aspects that cannot be observed directly, e.g. hydrodynamics in melt. It is crucial to describe electromagnetic field as precisely as possible, because it influences the shape of phase boundaries as well as convection and dopant transport in melt. From the dopant field it is possible to obtain radial resistivity variation (RRV) in the grown single crystal [1]. This result is important for industrial crystal growing companies, which are interested to achieve better crystals, i.e., crystals with more homogeneous resistivity profiles.

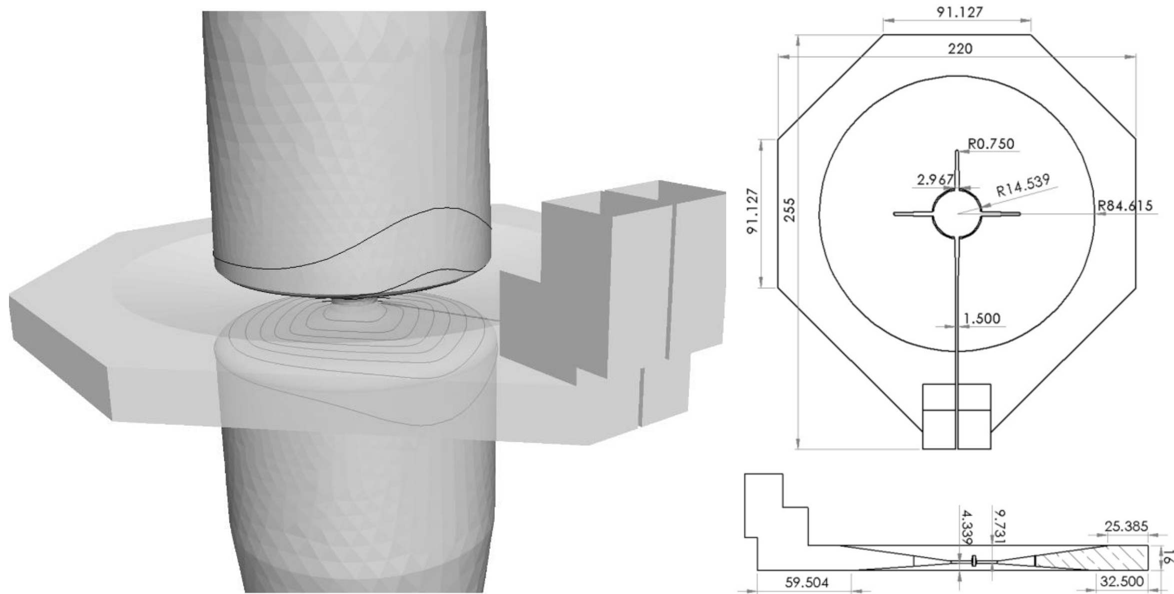

Figure 1. Left: overall view of 3D model of FZ system – feed rod, melt and crystal with current lines, and HF inductor. Right: drawings of the inductor (top and side views).

It is possible to improve and verify existing models of FZ process using new available experimental data. In the present work, the EM correction is introduced and verified by comparison with experiment. The influence of the electromagnetic field on phase boundaries, melt convection and dopant distribution in melt is presented and discussed. Main physical fields in melt are analysed, shape of crystallization interface and RRV profiles are compared with experimental data obtained from Institute for Crystal Growth, Berlin [2].

2. Mathematical models and software

A. Phase boundaries

2D axisymmetric calculations of phase boundaries are carried out using a specialized program *FZone* [3]. Since the skin depth varies between 0.038 mm for the copper inductor and 1.3 mm for the solid silicon, much less than the characteristic dimensions of the FZ system (≈ 0.1 m), the EM field distribution is determined by the surface current density. HF EM field is calculated considering the 3D HF inductor [4]. 3D induced EM surface power density distribution is azimuthally averaged and included in 2D axisymmetric phase boundary calculations as heat sources. Diffuse thermal radiation is taken into account using the axially symmetrical view factor model, considering all surfaces optically grey and opaque, with temperature-dependent emissivity. From the calculated temperature field and heat flux densities at the interfaces, the direction and magnitude of the movement of each interface point are obtained, and the quasi-stationary shape of phase boundaries is found iteratively. Free surface shape is found regarding the hydrostatical pressure, electromagnetic pressure, surface tension and centrifugal force. To obtain open melting front shape, thin fluid film model is used, assuming that feed rod melting is axially symmetrical [3].

B. EM correction

The HF approximation, which is described in [3], cannot be used when the exact distribution of volumetric EM field is important – for example, in the vicinity of solid-liquid interface, where skin depth changes by a factor of five. A local analysis of the EM field distribution in the vicinity of ETP (point position is shown in Figure 3) was carried out using the complex vector potential formulation. Internal triple point (ITP, its position is shown in Figure 3) was not considered due to the presence of thin melt film on the open front, that has

the same conductivity as the whole melt, and therefore EM field distribution is not changed there so dramatically.

A small domain near the ETP was considered. For the radial domain size much smaller than the crystal radius curvature in azimuthal direction can be neglected and 2D approximation can be used. Therefore all currents are flowing perpendicular to the *xz* (vertical) plane and the vector potential has only one component A_y. The following equation was numerically solved:

$$\Delta A_y - i\omega\sigma\mu A_y = 0,$$

where A_y is azimuthal component of the complex vector potential, i is the imaginary unit, ω = 2π·3 MHz is inductor current angular frequency, σ is silicon conductivity (5·10^4 S/m for solid and 1.2·10^6 S/m for liquid) and μ = 4π·10^{-7} N/A^2 is the magnetic constant. Boundary conditions were (see Figure 2, left):

a. $A_y = 0$ at the left boundary of the calculation domain;

b. $A_y = 1$ at the right boundary of the calculation domain (modelling the presence of inductor with fixed current that flows in *y* direction);

c. $\partial A_y / \partial n = 0$ at the top and bottom boundaries of the calculation domain (symmetry conditions).

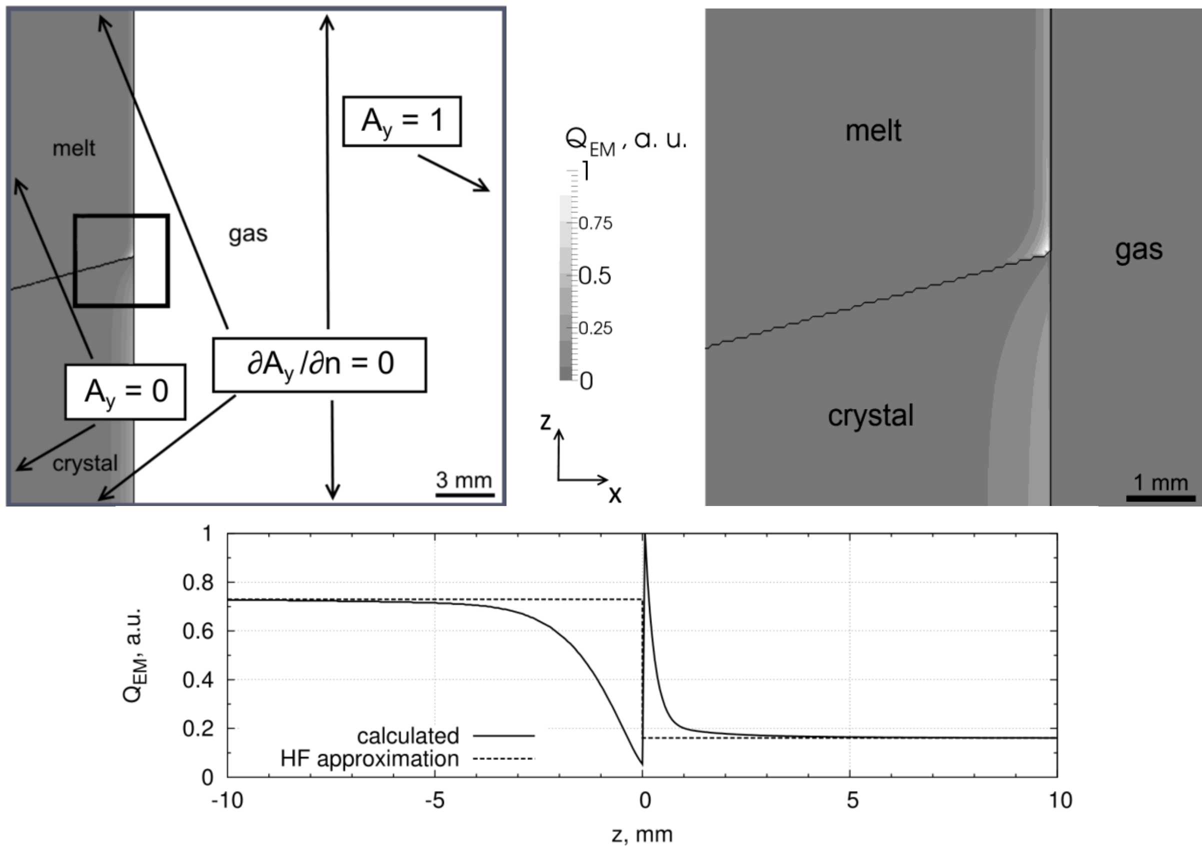

Figure 2. Top left: whole calculation domain with boundary conditions for vector potential. Top right: induced EM power density distribution in the vicinity of ETP (shown with the square on the left image), arbitrary units. Bottom: linear induced EM power as a function of vertical coordinate in melt (*z>0)* and crystal (*z<0)*, arbitrary units. Solid line shows the result calculated with vector potential formulation and dashed line – previously used HF approximation.

The equation was solved with finite difference method on a rectangular grid. The calculation domain of 24x24 mm^2 was divided in 400x400 points. It was obtained that in the first few millimetres near the ETP the actual induced EM power is significantly different from the induced EM power far from ETP (and thus different from the imprecise power distribution previously obtained by HF approximation). More power is induced in the melt and less in the crystal, see Figure 2, top right. By integrating the heat distribution along lines parallel to the crystal-melt interface, surface heat source density distribution is obtained (see Figure 2, bottom).

The result of local analysis was included in *FZone* as a correction to EM heat sources at free melt and crystal side surfaces. This correction was used only in axially symmetric calculation of phase boundaries as a correction to boundary conditions for temperature, not directly in 3D HF EM calculations. Because of changed EM heat sources in crystal and melt, inductor current needs to be adjusted to maintain the same zone height. The crystallization interface shape near the ETP changes due to the change of local heat sources; the change of shapes on global scale occurs due to different inductor current and integral induced power on the free melt surface.

C. 3D melt flow

The unsteady 3D melt flow in the FZ process is modelled using the open source code library *OpenFOAM*. For the considered system Reynolds number is roughly 1500, therefore the melt flow is considered as laminar. The detailed description of the mathematical model is given in [1], only the details relevant to the present study are summarized.

For incompressible melt flow, the Navier-Stokes equations are solved, and for description of buoyancy, the Boussinesq approximation is used. Boundary conditions for melt velocity are:

a. The crystallization interface is considered as a velocity outlet including constant mass outflow and crystal rotation.

b. The melting interface is considered as an inlet and the desired mass inflow is set equal to the outflow through the crystallization interface. A ring-shaped profile is used for the vertical velocity component to simulate melt flow from the open melting front through the thin melt film.

c. The distribution of the Marangoni surface force (obtained from temperature field, recalculated at every time step) and EM surface force distribution (acquired from the 3D HF EM calculations) are used to set boundary conditions for the melt velocity on the free melt surface: $f_s = \frac{1}{4}\mu_0\, \delta\, \nabla j^2 + M\, \nabla T$, where f_s is the surface force, $\delta = \frac{1}{\sqrt{\pi f_{\mathrm{ind}} \sigma \mu_0}}$ is the skin depth, ∇ is the surface gradient, j is the surface current density, M = -1.3·10^{-4} N/(m K) is the Marangoni coefficient, T is the temperature, f_{ind} is the inductor current frequency and σ is the conductivity of liquid silicon. Marangoni force is directed from higher to lower temperatures, while EM force, F_{EM}, – typically in the opposite direction.

Temperature field is governed by non-stationary convection-diffusion equation. The corresponding boundary conditions are the following:

a. Fixed temperature, equal to melting point of silicon (1687 K), on melting and crystallization interfaces.

b. Fixed heat flux density, equal to sum of radiative heat losses (negative) approximated from axially symmetrical *FZone* [3] calculations and induced EM power density, on melt free surface.

For the dopant concentration field, *C,* the mass transport equation is solved. From the calculated *C* distribution at the crystallization interface the resistivity of grown crystal, ρ, can

be obtained: $\rho = 1/(k_0 C)$, where k_0=0.35 is the segregation coefficient. The boundary conditions are:

a. On the crystallization interface $D\frac{\partial C}{\partial n} = v_c(1-k_0)C\cos\theta$, where n is the normal direction, v_c is crystal pulling speed and θ is the angle between the XY (horizontal) plane and the interface normal vector.

b. On the melt free surface due to the assumption of homogeneous concentration distribution in argon atmosphere a fixed concentration is applied, normalized to $C = 1$.

c. On the melting interface – ring-shaped profile, where dopant concentration at ring is equal to concentration on free surface, and silicon feed rod is considered pure ($C = 0$).

3. Calculation results

Phase boundaries of the considered 4" FZ system with crystal pulling rate v_c = 3.4 mm/min (detailed information about system parameters and geometry of inductor can be found in [5]) are calculated using program *FZone* and shown in Figure 3 on the left. When EM correction is included, higher inductor current, I_0, is required to hold prescribed zone height (32.5 mm) and it leads to larger deflection of crystallization interface, H_C, see Table 1. This shape is closer to the experimental one. Induced EM power density and force vectors for different inductor current frequency are shown in Figure 3 on the right. Heat sources are approximately the same, because calculation algorithm is maintaining fixed zone height. F_{EM} is significantly different: maximal values are 0.49 N/m^2 for 3 MHz and 0.70 N/m^2 for 2 MHz.

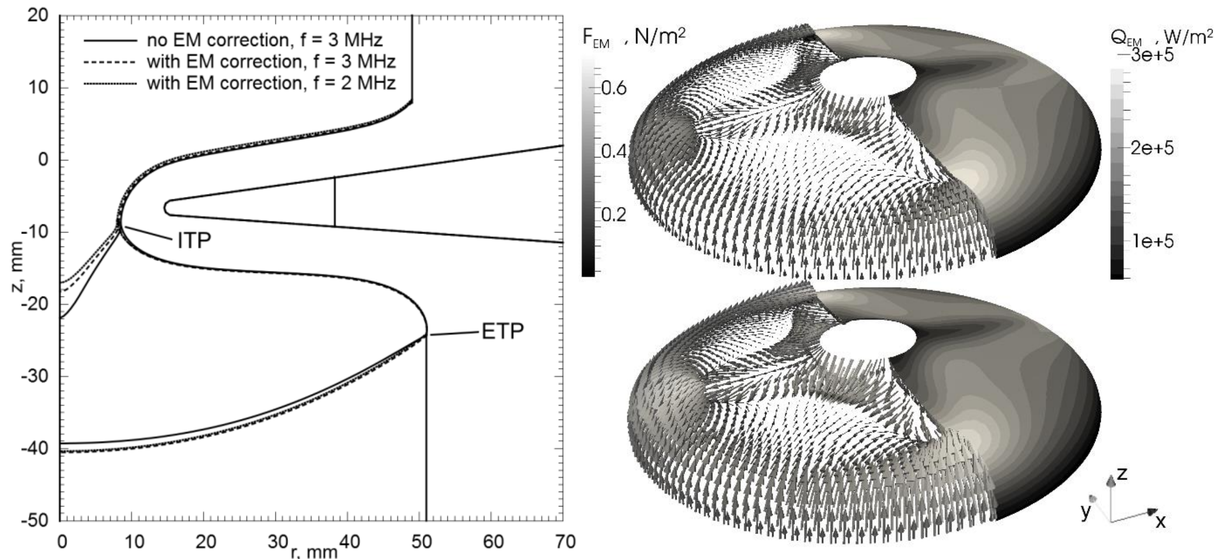

Figure 3. Left: phase boundaries of considered system for various EM fields. Also shown are the ETP and ITP. Right: EM heat sources and EM force on free melt surface for cases with EM correction for different inductor current frequency (top – 3 MHz, bottom – 2 MHz). Current inlets are located in the positive direction of x axis.

Case	I_0, A	H_C, mm
No EM correction, f_{ind} = 3 MHz	870	15.0
With EM correction, f_{ind} = 3 MHz	884	16.2
With EM correction, f_{ind} = 2 MHz	953	16.3

Table 1. Results of phase boundary calculations.

Using the obtained axisymmetric shape of phase boundaries, 3D HD calculations were performed on a block-structured mesh consisting of 80 000 hexahedral elements. As a result, non-stationary physical fields are obtained. Nevertheless, phase boundaries are fixed, so transient behaviour and control of FZ control process is not taken into account in these calculations, and unsteady behaviour can be expressed only in characteristic oscillations. Melt velocity and temperature oscillations at the particular probe point near the crystallization interface are shown in Figure 4. Approximate oscillation period is the same for both fields, about 2-3 s. As there are no qualitative differences between the cases with and without EM correction, it can be concluded that use of correction does not significantly change time-dependent behaviour of the present numerical model.

A sample of calculated fields, averaged over 5 s interval at the end of HD calculations – melt velocity, temperature and dopant concentration – is shown in Figures 5, 6 and 7. Two characteristic temperature maxima on the free melt surface are formed below the additional slits of inductor due to non-symmetric induced heat sources (see Figure 3). Therefore, the lowest temperature occurs below the main slit of inductor.

Velocity field in the vertical slice of the melt (see Figure 7) shows that near the ETP electromagnetic forces are dominating and creating a distinct vortex. As it frequently happens in 4” FZ system, dopant concentration maximum is formed by two vortexes, swirled in opposite directions – the first one occurs due to the vertical motion of melt from the crystallization interface and the second is created by the EM force on the free surface. When the inductor frequency is lowered to 2 MHz, the velocity field in the considered vertical slice becomes more asymmetric and less stable (i.e., stronger fluctuations in time), which leads to the more intensive mixing processes. On the other hand, top view of the free surface shows a distinct asymmetry of the velocity field, see Figure 6. It means that the melt velocity in a vertical slice can only partially represent processes in the whole melt.

To investigate the influence of EM forces on melt motion more precisely, the distribution of tangential melt velocity component (projected on the plane of the slice) is shown in Figure 8. As the EM force becomes higher for lower inductor frequency, the melt velocity considerably increases. Both near the ETP and ITP (for definition, see Figure 3) melt flow becomes stronger in the direction from lower to higher temperatures. It means that for the lower inductor frequency the EM force is stronger than the Marangoni force, excluding very small region near the ITP. Moreover, the temperature profile on the free surface (see Figure 9) indicates a more intense mixing in melt, which leads to low temperature gradients and low Marangoni force.

One more important process is the reverse of a vortex in the vicinity of ETP, when EM forces are turned off. In Figure 8 it can be seen that the tangential velocity component swiped from positive to negative, and this direction corresponds to the direction of Marangoni convection – from higher to lower temperatures. This tendency is very pronounced in the vicinity of ITP, too.

Finally, from the concentration distribution on the crystallization interface RRV profiles are obtained (see Figure 10). Table 2, which summarizes sum of squared differences between experimental and calculated RRV profiles, shows that the case with EM correction and f_{ind} = 3 MHz describes experimental data more precisely than others. Experimental data was obtained using f_{ind} = 3 MHz, and the expected result that calculation with f_{ind} = 2 MHz has a significantly worse agreement with experiment indicates that the used system of numerical models is sensitive to inductor current frequency. For f_{ind} = 2 MHz, resistivity minimum was shifted towards the crystal axis due to a changed structure of vortexes, and the whole profile became flatter due to a more intense convection in the melt (see Figure 7). It can be concluded that RRV profiles are very sensitive on the changes in melt flow, so that

they can respond even on small velocity differences and can be used to verify EM correction and other possible improvements in boundary conditions and calculation process.

4. Conclusions

It was shown that EM field has significant influence both on the shape of phase boundaries and on melt hydrodynamics. EM correction allows to describe phase boundaries more precisely, and it leads to changes in RRV profile, even although influence of correction is considered only through the change of phase boundaries, not including it in temperature boundary conditions for 3D melt flow calculations. Position of resistivity minima became closer to experimentally observed and the sum of squared differences diminished, therefore EM correction improved models' qualitative and quantitative correspondence to experiment.

When calculations are performed without EM forces, distribution of velocity on melt free surface shows that Marangoni force reverses vortices near ETP, and additional resistivity minimum occurs. Clear influence of the lowering of inductor current frequency was detected due to the significant increment of EM forces – resistivity minimum shifted towards the crystal axis, and RRV profile became more flat. The next aim of the study could be implementation of EM correction in 3D HF EM calculation program, which creates EM heat sources – boundary conditions for melt flow calculations, to observe direct influence of EM correction on the 3D melt flow and dopant distribution. One more possibility is to use correction not only for heat sources, but also for EM force distribution.

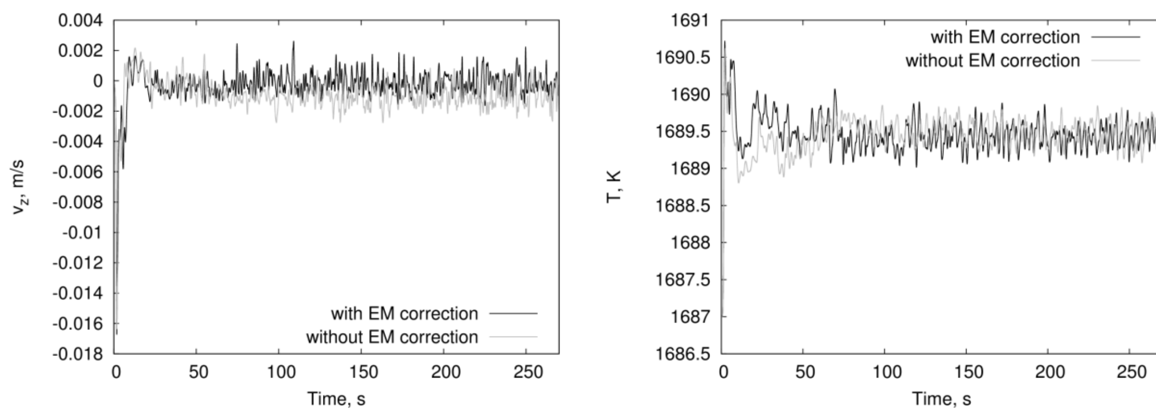

Figure 4. Oscillations of melt velocity vertical component (left) and temperature (right) at the probe point, located 1 mm above the crystallization interface at $x = 0$ and $y = 25$ mm.

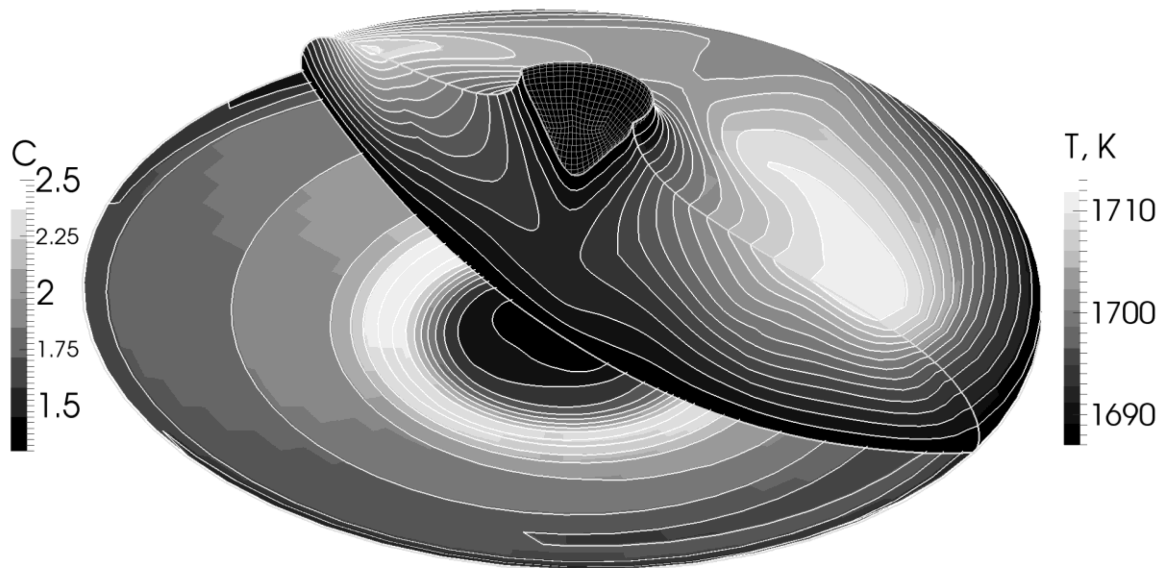

Figure 5. Crystallization interface and vertical cut of the melt. Melt temperature is shown in the right part of melt; dopant concentration is depicted on crystallization interface. On melting interface mesh edges are shown. Calculation example with EM correction and f_{ind} = 3 MHz.

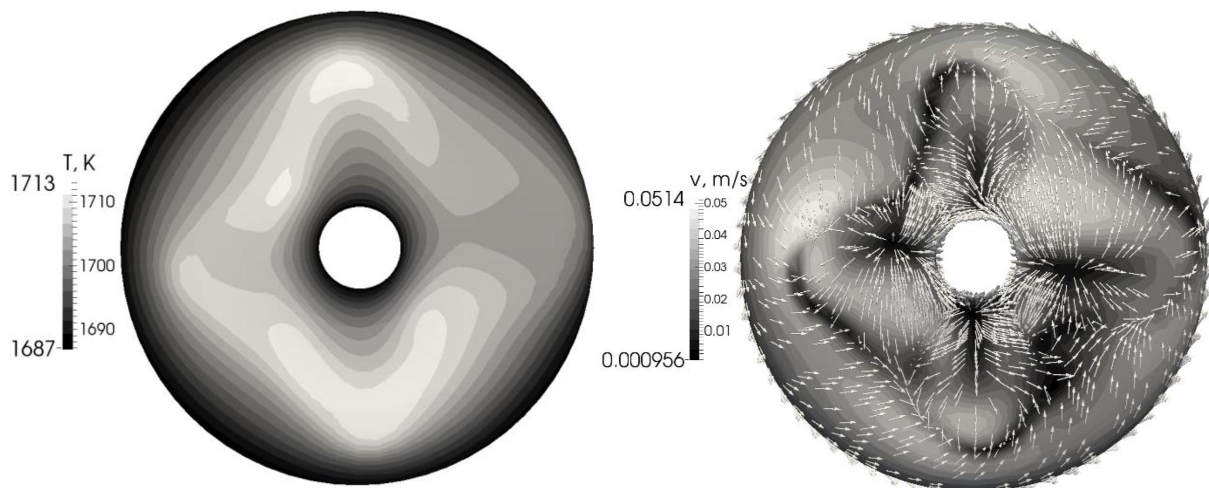

Figure 6. Top view of melt free surface with temperature (left) and velocity (right). Calculation example with EM correction and f_{ind} = 3 MHz.

No EM correction, f_{ind} = 3 MHz	With EM correction, f_{ind} = 3 MHz	With EM correction, no EM forces	With EM correction, f_{ind} = 2 MHz
0.80	0.38	0.88	2.11

Table 2. Sum of squared differences (deviations) between experimental (obtained with f_{ind} = 3 MHz) and calculated RRV profiles, in arbitrary units.

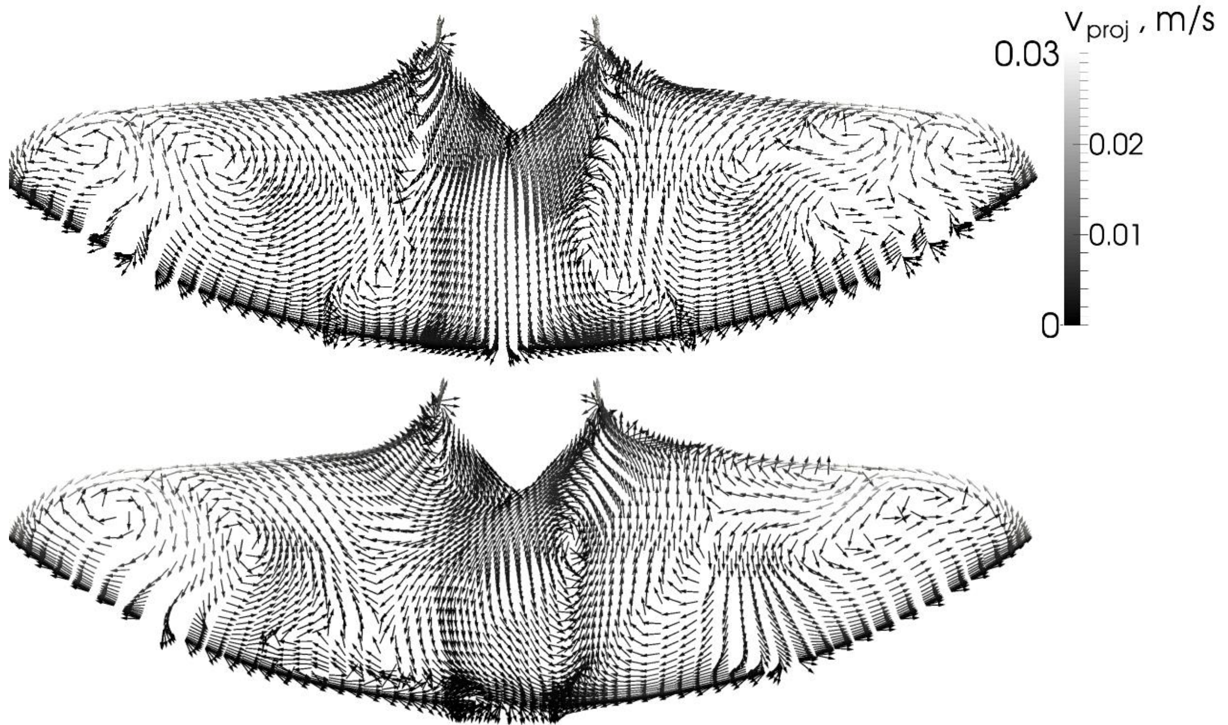

Figure 7. Time-averaged melt velocity projection on the vertical slice of the melt, perpendicular to inductor current suppliers. Top – f_{ind} = 3 MHz, bottom – f_{ind} = 2 MHz

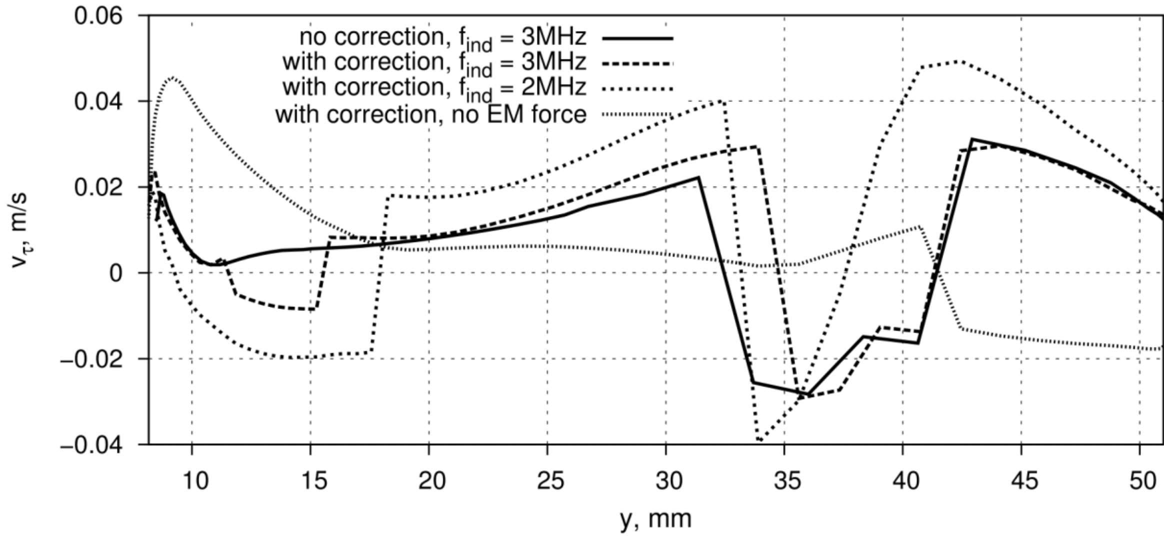

Figure 8. Distribution of in-plane velocity on melt free surface. y is horizontal coordinate perpendicular to inductor current suppliers, 51 mm corresponds to ETP.
v_τ is defined as positive if melt moves towards the crystal axis.

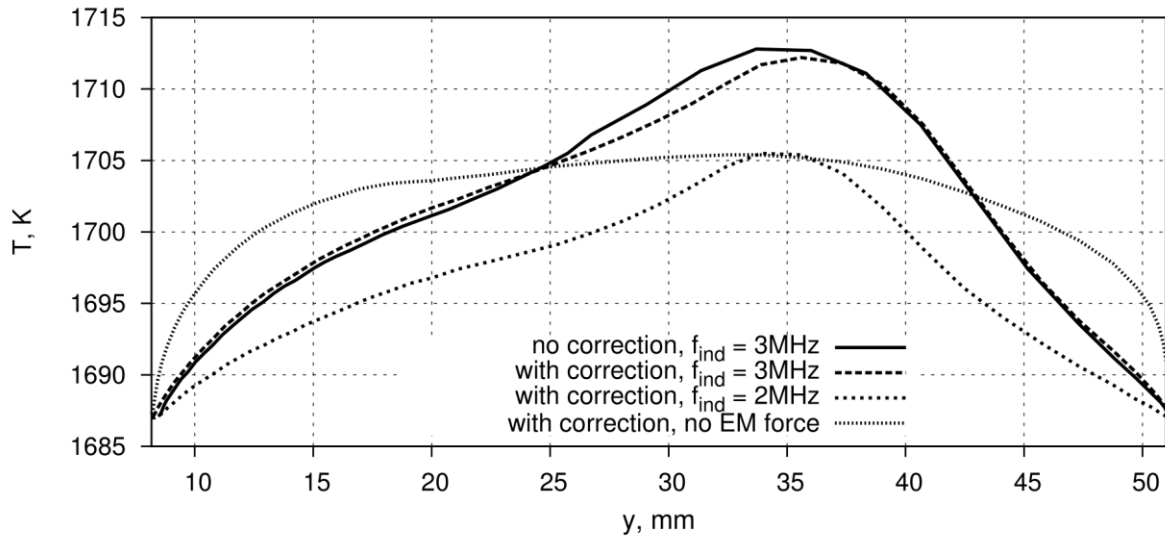

Figure 9. Distribution of temperature on melt free surface. *y* is horizontal coordinate perpendicular to inductor current suppliers, 51 mm corresponds to ETP.

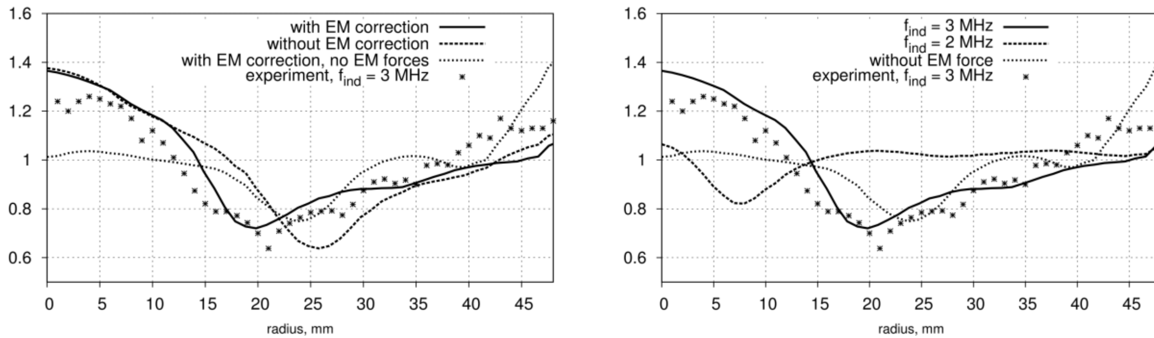

Figure 10. RRV profiles. Resistivity is normalised to its average and displayed in arbitrary units. Left: $f_{\mathrm{ind}} = 3$ MHz, right: calculations on the mesh obtained with EM correction.

5. Acknowledgments

This work has been supported by the European Regional Development Fund, project Contract no. 2013/0051/2DP/2.1.1.1.0/13/APIA/VIAA/009.

5. References

[1] Lacis, K.; Muiznieks, A.; Rudevics, A.; Sabanskis, A.: Influence of DC and AC magnetic fields on melt motion in FZ large Si crystal growth. Magnetohydrodynamics. 46 (2010) 119-218.
[2] Rost, H.-J.; Menzel, R.; Luedge, A.; Riemann, H.: FZ silicon crystal growth at reduced RF frequencies. Journal of Crystal Growth. 360 (2012) 43-46.
[3] Ratnieks, G.; Muiznieks, A.; Muhlbauer, A: Modelling of phase boundaries for large industrial FZ silicon crystal growth with the needle-eye technique. Journal of Crystal Growth. 255 (2003) 227-240.
[4] Muiznieks, A.; Rudevics, A.; Riemann, H.; Lacis, U.: Comparison between 2D and 3D modelling of HF electromagnetic field in FZ silicon crystal growth process. International Scientific Colloquium Modelling for Material Processing, Riga. (2010) 61-65.
[5] Surovovs, K.; Muiznieks, A.; Sabanskis, A.; Virbulis, J.: Hydrodynamical aspects of the floating zone silicon crystal growth process. Journal of Crystal Growth, 401 (2014) 120-123.